Binary neutron star mergers and short gamma-ray bursts: Effects of magnetic field orientation, equation of state, and mass ratio

Takumu Kawamura, Bruno Giacomazzo,[*] Wolfgang Kastaun, Riccardo Ciolfi, and Andrea Endrizzi

Physics Department, University of Trento, via Sommarive 14, I-38123 Trento, Italy
and INFN-TIFPA, Trento Institute for Fundamental Physics and Applications,
via Sommarive 14, I-38123 Trento, Italy

Luca Baiotti

Graduate School of Science, Osaka University, Toyonaka, 560-0043, Japan

Rosalba Perna

Department of Physics and Astronomy, Stony Brook University, Stony Brook, New York 11794-3800, USA

We present fully general-relativistic magnetohydrodynamic simulations of the merger of binary neutron star (BNS) systems. We consider BNSs producing a hypermassive neutron star (HMNS) that collapses to a spinning black hole (BH) surrounded by a magnetized accretion disk in a few tens of ms. We investigate whether such systems may launch relativistic jets and hence power short gamma-ray bursts. We study the effects of different equations of state (EOSs), different mass ratios, and different magnetic field orientations. For all cases, we present a detailed investigation of the matter dynamics and of the magnetic field evolution, with particular attention to its global structure and possible emission of relativistic jets. The main result of this work is that we observe the formation of an organized magnetic field structure. This happens independently of EOS, mass ratio, and initial magnetic field orientation. We also show that those models that produce a longer-lived HMNS lead to a stronger magnetic field before collapse to a BH. Such larger fields make it possible, for at least one of our models, to resolve the magnetorotational instability and hence further amplify the magnetic field in the disk. However, by the end of our simulations, we do not (yet) observe a magnetically dominated funnel nor a relativistic outflow. With respect to the recent simulations of Ruiz *et al.* [Astrophys. J. **824**, L6 (2016)], we evolve models with lower and more plausible initial magnetic field strengths and (for computational reasons) we do not evolve the accretion disk for the long time scales that seem to be required in order to see a relativistic outflow. Since all our models produce a similar ordered magnetic field structure aligned with the BH spin axis, we expect that the results found by Ruiz *et al.* (who only considered an equal-mass system with an ideal fluid EOS) should be general and—at least from a qualitative point of view—independent of the mass ratio, magnetic field orientation, and EOS.

I. INTRODUCTION

With the revolutionary first detections of gravitational waves (GWs) by Advanced LIGO [1,2] from the merger of compact binary systems composed of two black holes (BHs), there have been even greater expectations of possible near-future detections of other sources, including binaries composed either of two neutron stars (NSs) or of a NS and a BH. While solar-mass binary BH mergers are not expected to emit electromagnetic (EM) signals (but see, e.g., Refs. [3–5] for possible alternatives), binary neutron star (BNS) and NS-BH systems are considered very powerful sources of a variety of EM counterparts, ranging from collimated emission [such as short gamma-ray bursts (SGRBs)] to more isotropic ones (such as the so-called kilonova/macronova) [6–8].

In particular, the possibility that SGRBs are powered by BNS or NS-BH mergers is supported by observational evidence (see Ref. [9] for a recent review). The simultaneous detection of a SGRB and GWs from a BNS or a NS-BH merger would represent definitive proof that these binary mergers power the central engine of SGRBs. Moreover, this association could provide strong constraints on the equation of state (EOS) of NS matter [10].

One of the leading theoretical models describing the gamma-ray emission in SGRBs is based on the launch of a relativistic jet from a spinning BH surrounded by an accretion disk. Jets may be launched via neutrino-antineutrino annihilation [11–13] or via magnetic mechanisms, such as the Blandford-Znajek (BZ) mechanism [14]. While fully general relativistic simulations of BNS mergers have shown that (in those cases where the merger results in BH formation on a dynamical time scale) disks as massive as $\sim 0.1 M_\odot$ can be easily formed [15], whether the emission of relativistic jets occurs or not is still under investigation.

[*]bruno.giacomazzo@unitn.it

This has driven an increasing effort in performing fully general-relativistic magnetohydrodynamic (GRMHD) simulations of BNS mergers, with the first simulations dating back to a few years ago [16–18]. More recently some groups started to investigate the formation of jets [19–22]. The simulation by Rezzolla *et al.* [20] was in particular the first to show the possibility of forming an ordered and mainly poloidal magnetic field configuration aligned with the BH spin axis. Even if no outflow was observed, this provided a strong indication that BNS mergers can at least provide some of the necessary conditions to launch a relativistic jet. A subsequent simulation by Kiuchi *et al.* [21], using a different EOS, has challenged that result. Meanwhile, both local and global simulations of magnetic field evolution in the merger of BNS systems have shown that very large fields of up to $\sim 10^{16}$ G can be formed during merger [23–25]. Since it was shown that the formation of a magnetically dominated region in the BH ergosphere is a necessary condition for the activation of the BZ mechanism [26], these new results encouraged further studies. Very recently, GRMHD simulations by Ruiz *et al.* [19] have shown that, when starting with very large magnetic fields, it is possible to observe the formation of a mildly relativistic outflow few tens of ms after BH formation. Even if the initial magnetic fields were unrealistically large, i.e., $\sim 10^{15}$ G, such fields should be produced after merger and therefore these simulations provide a proof of concept that jets may indeed be launched. Moreover, these recent simulations have shown that jets may be launched even when considering magnetic fields confined inside the NSs.

All previous simulations considered only equal-mass systems and only two EOSs: ideal fluid [19,20] or piecewise polytropic [21]. In this paper we extend the previous investigations by studying—with our GRMHD code WHISKY [27–29]—the magnetic field structure that is formed after the merger of BNS systems and how it depends on the initial mass ratio, EOS, and initial magnetic field orientation. As such, our work allows us to assess the robustness of previous results when these important parameters are changed and we consider this as a preliminary step before performing simulations with very high resolutions or using our subgrid model [24] to further study the effect of large magnetic field amplifications. All our simulations start with plausible values for the initial magnetic field, i.e., $\sim 10^{12}$ G. The role of neutrino emission is not included in our simulations and we believe that this does not affect our results qualitatively. We are currently working on the implementation of neutrino treatment in our GRMHD code and we point out that up to now only one recent work has presented GRMHD simulations of BNS merger including magnetic fields, neutrino emission, and a finite-temperature EOS [30].

Our paper is organized as follows. In Sec. II we describe our numerical setup and in Sec. III we describe the initial data used in our simulations. We remark that our equal-mass models are the same as those that were evolved by Rezzolla *et al.* [20] and Kiuchi *et al.* [21], while the unequal-mass ones are studied here for the first time. In Sec. IV we describe in detail the evolution of our different initial models, for the first time with a very accurate description of the magnetic field configurations formed after merger (implementing also advanced visualization tools that are described in the Appendix). In Sec. V we discuss the connection with SGRBs and other possible EM counterparts, while in Sec. VI we present the GW signal. In Sec. VII we conclude and summarize the main results of our work.

We use a system of units in which $G = c = M_\odot = 1$ unless specified otherwise. The time is shifted so that $t = 0$ refers to the time of merger, which corresponds to the maximum amplitude in the GW signal.

II. NUMERICAL METHODS

All the simulations discussed in this paper made use of the publicly available Einstein Toolkit [31] coupled with our fully GRMHD code WHISKY [27–29].

Our version of the WHISKY code solves the GRMHD equations on a dynamically curved background by using the "Valencia" formulation [32]. In order to satisfy at all times the divergence-free condition of the magnetic field, we evolve the vector potential and then recompute the magnetic field from it at each time step. In order to avoid spurious magnetic field amplifications at the boundary between refinement levels we use the "modified Lorenz gauge" as described in Refs. [33,34]. The fluxes at the interfaces between numerical cells are computed using the HLLE approximate Riemann solver [35] that takes as input the values of the primitive variables reconstructed with the piecewise-parabolic method [36]. We also set the floor value for the rest-mass density ρ to $10^{-13} \approx 6.2 \times 10^4$ g cm^{-3}. When ρ decreases below that level, we reset it to the floor value (which we also call the artificial atmosphere) and we also set the velocity to be zero. After BH formation we excise the hydrodynamic variables in the region inside the apparent horizon (by setting them to the values they have in the artificial atmosphere) in order to prevent failures in the conservative to primitive routines due to the high-level of magnetization that may be reached inside the BH. More technical details about our GRMHD WHISKY code can be found in our previous publications [27–29,37].

In this work, the WHISKY code is coupled with version ET_2014_05 (codename "Wheeler") of the Einstein Toolkit. The latter is a collection of publicly available routines for numerical relativity simulations on supercomputers. In particular, for the evolution of the spacetime we used the BSSNOK [38–40] formulation as implemented in the McLachlan code. We also used the adaptive mesh refinement driver Carpet with a total of six refinement levels. The finest grids cover each of the NSs during the inspiral and, after merger, they are merged into a larger one that covers the resulting hypermassive NS (HMNS). We

adopted a resolution on the finest grids of ≈ 222 m in the runs using an ideal-fluid EOS and of ≈ 186 m in the runs using the H4 EOS. This choice has been made so that the NSs are covered by approximately the same number of points in both cases. The external boundary is located at a distance of ≈ 1400 km in the ideal-fluid case and ≈ 1200 km in the H4 case. All the simulations employed reflection symmetry across the equatorial plane to reduce computational costs.

III. INITIAL DATA

We evolve magnetized, quasicircular and irrotational BNS models. The main properties of the initial data used for our simulations are listed in Table I. These data are produced using the spectral-method code LORENE (http://www.lorene.obspm.fr), except for the setup of the magnetic field (see below). We employ the ideal-fluid EOS (denoted IF in the table) and the H4 EOS (denoted H4 [41]), along with poloidal initial magnetic fields that are confined inside the stars. The ideal-fluid EOS uses a polytropic index $\Gamma = 2$ and a polytropic constant $K = 100$ as in previous simulations [20,28]. The H4 EOS is instead implemented as a piecewise polytropic EOS as described in Ref. [42]. In order to also take thermal effects into account in this case, we add a thermal part via an ideal-fluid EOS with a polytropic index $\Gamma = 1.8$ as done in Refs. [21,25]. The total masses have been chosen so that the ideal-fluid and H4 equal-mass models are the same as the ones evolved in Ref. [20] and Refs. [21,25], respectively. All our models inspiral for ~ 3–6 orbits before merger. Time of merger is defined as the time of maximum amplitude in the GW signal.

For the ideal-fluid equal-mass simulations, we use three different magnetic field orientations: both NS magnetic fields aligned to the orbital rotation axis (UU), aligned and antialigned (UD), and both antialigned (DD). For the ideal-fluid unequal-mass simulation, and also for the H4

equal- and unequal-mass simulations, we use the UU magnetic field configuration. In summary, there are six models according to EOSs, mass ratio, and magnetic field configurations: IF_q10_UU, IF_q10_UD, IF_q10_DD, IF_q08_UU, H4_q10_UU, and H4_q08_UU. All the initial data computed with LORENE are publicly available online [43], except for model IF_q10 (ideal-fluid equal-mass) which is already available on the LORENE web page as model G2_I14vs14_D4R33_45km.

The magnetic fields are added *a posteriori* on top of the initial data produced with LORENE using the following vector potential:

$$A_\phi \equiv \varpi^2 A_b \max(p - p_{\mathrm{cut}}, 0)^{n_{\mathrm{s}}}, \qquad (1)$$

where ϖ is the coordinate distance from the NS spin axis, $p_{\mathrm{cut}} = 0.04 \max(p)$ is a cutoff that determines where the magnetic field goes to zero inside the NS, $\max(p)$ is the initial maximum pressure in each star, and $n_{\mathrm{s}} = 2$ is the degree of differentiability of the magnetic field strength [28]. The values for A_b for each model are listed in Table I. For the unequal-mass models different values for A_b were used for each star in order to guarantee that they had the same initial magnetic field strength. Antialigned fields are instead obtained by multiplying A_b by -1.

IV. EVOLUTION

In this section we provide an extensive discussion of the results of our simulations, including the general dynamics, the magnetic field evolution, the dependence on the EOS and the mass ratio, a comparison with previous work, and a resolution study. The connection to SGRBs and GW emission are discussed in Secs. V and VI. Important quantities characterizing the system are summarized in Table II for the different cases considered in this work.

TABLE I. Initial data parameters: mass ratio ($q = M_{\mathrm{g}}^1 / M_{\mathrm{g}}^2$), total baryonic mass of the system ($M_{\mathrm{b}}^{\mathrm{tot}}$), baryonic and gravitational masses of each star at infinite separation (M_{b} and M_{g}), compactness (M_{g}/R_c, dimensionless), initial orbital frequency and proper separation (f_0 and d), initial magnetic energy (E_B), initial maximum value of magnetic field strength (B_{max}), and A_b, the value in geometric units used in Eq. (1) in order to fix B_{max}.

Model	IF equal	IF unequal	H4 equal	H4 unequal
q	1	0.816	1	0.816
$M_{\mathrm{b}}^{\mathrm{tot}}$ [$M_\odot$]	3.25	3.25	3.04	3.04
M_{b} [$M_\odot$]	1.63	1.44, 1.81	1.52	1.35, 1.69
M_{g} [$M_\odot$]	1.51	1.36, 1.67	1.40	1.26, 1.54
M_{g}/R_c	0.140	0.120, 0.164	0.148	0.132, 0.164
f_0 [Hz]	295	234	263	263
d [km]	59.3	68.0	61.0	61.0
E_B [10^{40} erg]	8.19	8.03	9.51	9.32
B_{max} [10^{12} G]	1.99	1.99	1.99	1.99
A_b	2.20	0.76, 5.36	1.97	1.21, 3.13

TABLE II. System properties for the different EOS and mass ratios considered in this work: BH mass (M_{BH}), spin (a_{BH}), and disk mass (M_{disk}) at the end of our simulations (27–30 ms after collapse), accretion rate ($\dot{M}$), accretion time scale ($\tau_{acc} \equiv M_{disk}/\dot{M}$, time of BH formation since merger (t_{BH}), instantaneous GW frequency at merger (f_{merger}), and characteristic GW frequency in the HMNS phase (f_{HMNS}). The accretion rate is taken as the time average from 5 ms after collapse to the end of the simulation. The time of merger $t = 0$ corresponds to the maximum GW strain. f_{HMNS} is estimated from the characteristic peak in the post-merger spectrum (see Sec. VI).

Model	IF equal	IF unequal	H4 equal	H4 unequal
M_{BH} [$M_\odot$]	2.92	2.78	2.67	2.50
a_{BH}	0.81	0.77	0.71	0.63
M_{disk} [$M_\odot$]	0.04	0.21	0.04	0.23
$\dot{M}$ [$M_\odot/s$]	0.8	2.6	1.1	1.8
τ_{acc} [s]	0.05	0.08	0.03	0.13
t_{BH} [ms]	8.7	1.3	11.6	24.7
f_{merger} [kHz]	1.36	0.96	1.43	1.62
f_{HMNS} [kHz]	$\cdots$	$\cdots$	2.47	2.69

A. Ideal-fluid equal-mass model

We first consider the equal-mass case with ideal-fluid EOS and initial magnetic fields aligned with the orbital axis, `IF_q10_UU`. The following discussion refers to the standard resolution simulation, while different resolutions for this case are considered in Sec. IV H.

The rest-mass density evolutions on the equatorial and meridional planes are shown in the top rows of Figs. 1

and 2, respectively. As its total rest mass is well within the hypermassive regime for a single object, the merger is followed by a HMNS phase lasting ~8.5 ms and the eventual collapse to a BH. Most of the rest mass in the system is rapidly swallowed by the BH during its formation, leaving behind only a light disk. At the end of the simulation (~26 ms after BH formation) the disk mass is only ~0.04 $M_\odot$ and the accretion time scale is less than 100 ms (see Table II). The BH spin is relatively high, $a_{BH} \sim 0.8$ (the highest value obtained in this study).

The evolutions of the magnetic field energy and strength are shown in Figs. 3–5, and 6. A sudden increase of magnetic energy is observed in the first 2 ms after merger. This is to be attributed to the shear that is generated when the two stars first touch and that is associated with strong magnetic field amplification via the Kelvin-Helmholtz instability (although our resolution does not allow us to fully resolve it; see Sec. IV H). In the following evolution, the magnetic field is further amplified (at a lower rate) in the HMNS phase and in the remnant disk after BH formation. The magnetic energy and the maximum field strength do not show a sudden decrease at BH formation, indicating that most of the field is outside the high-density bulk of the HMNS that is immediately swallowed by the nascent BH. Conversely, such a drop is observed when considering a density-weighted average of the magnetic field strength. Around 15 ms after BH formation the gain in magnetic energy becomes lower than the loss associated with the accretion of magnetized material in the disk. Overall, the maximum magnetic field strength achieved is a
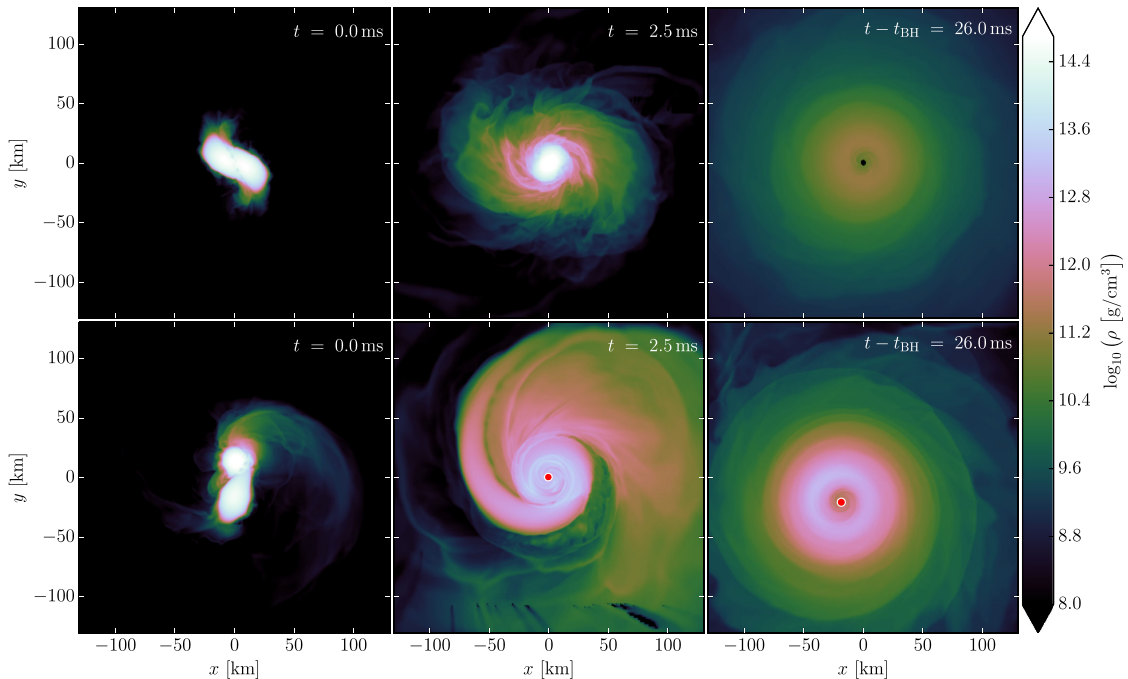

FIG. 1. Rest-mass density evolution on the equatorial plane for models `IF_q10` (top) and `IF_q08` (bottom). The horizon is marked with a red circle, with the exception of the top right panel which shows the excised region (black) instead.
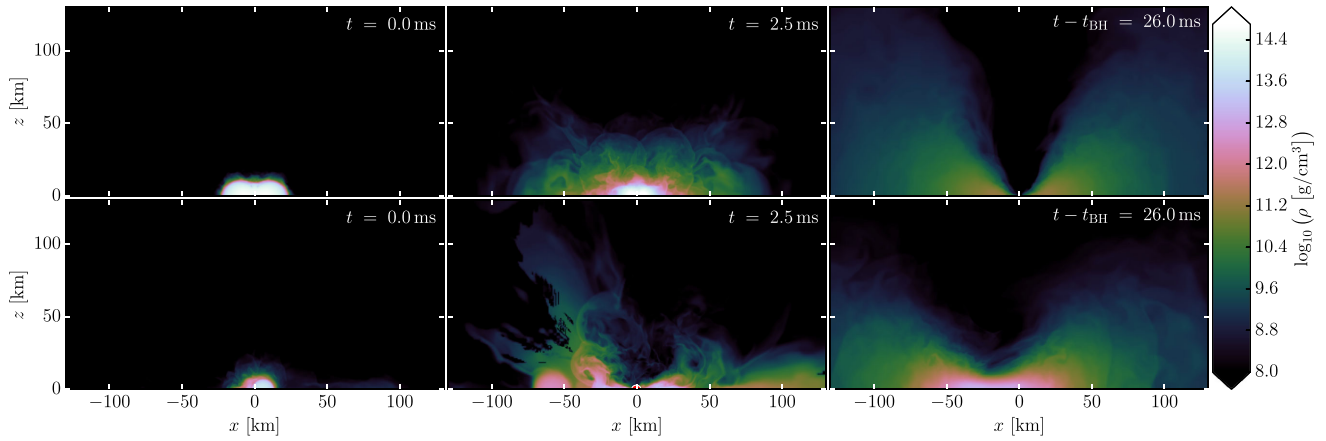
FIG. 2.   Rest-mass density evolution on the meridional plane for models IF_q10 (top) and IF_q08 (bottom). Note the lower right panel constitutes an off-center cut because of the BH drift.
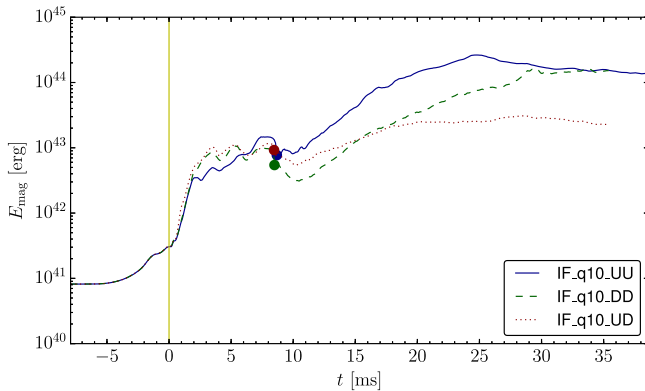

FIG. 3.   Comparison of the total magnetic energy between the models IF_q10_UU, IF_q10_DD, and IF_q10_UD. The yellow vertical line marks the merger time and the circles show the time of BH formation for each model.
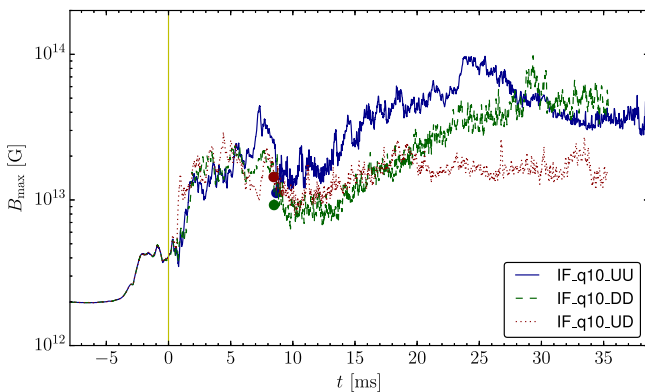
factor of ~ 50 higher than the initial value. More details on the magnetic field amplification mechanisms and the dependence on resolution are discussed in Sec. IV H.

As shown in Fig. 6, magnetic field amplification is mostly in favor of the toroidal component. In terms of average magnetic field strength, the toroidal component becomes comparable to the poloidal one in the first ms after merger and in the HMNS phase the two keep growing together. Then, after BH formation the poloidal field remains much smaller than the toroidal one, which is more efficiently amplified in the disk.

We now discuss in more detail the geometrical structure of the magnetic field. To qualitatively assess the global structure of the field, we use three-dimensional (3D) plots of selected field lines. Visualizing field lines is a complex task and can be very misleading. We developed a prescription for the automated selection of field lines that gives good results without any manual (i.e., potentially biased)

FIG. 4.   Comparison of the maximum values of the magnetic field strength between the models IF_q10_UU, IF_q10_DD, and IF_q10_UD. The yellow vertical line marks the merger time and the circles show the time of BH formation for each model.
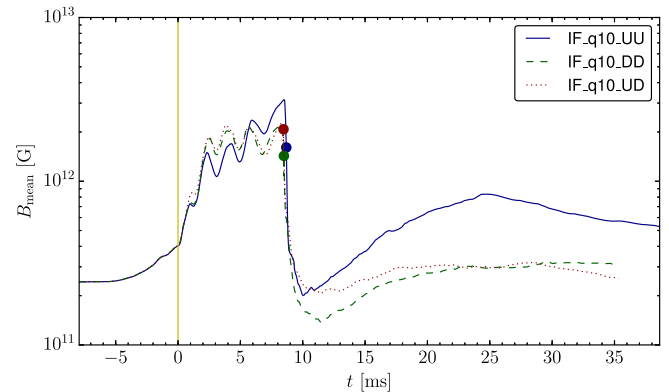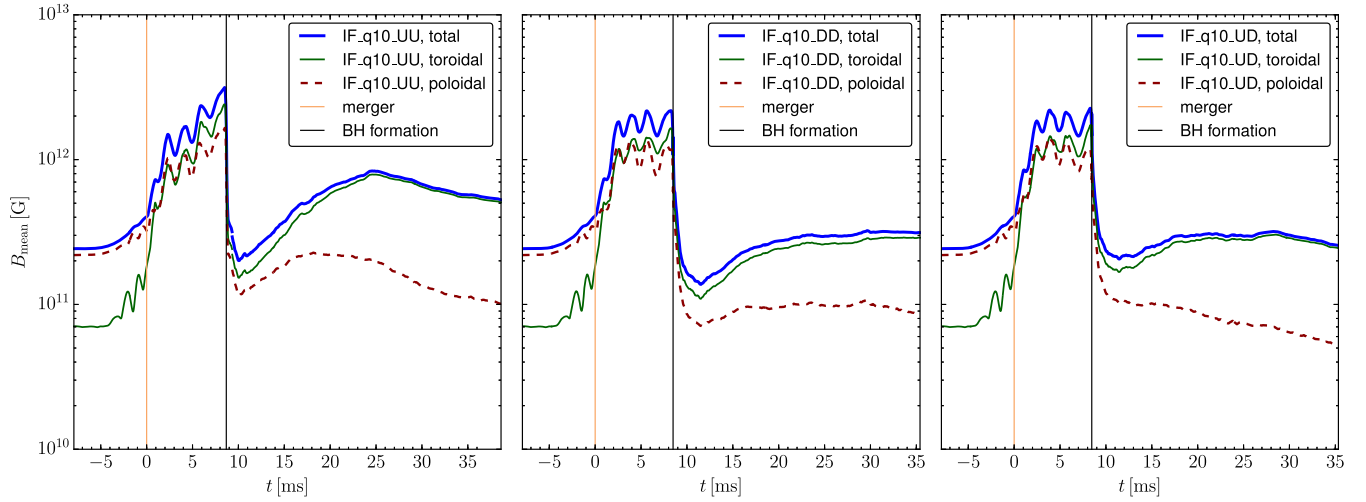

FIG. 5.   Comparison of the mean values of the magnetic field strength between the models IF_q10_UU, IF_q10_DD, and IF_q10_UD. The yellow vertical line marks the merger time and the circles show the time of BH formation for each model.

FIG. 6.   Comparison of the mean values of the magnetic field strength between the models `IF_q10_UU`, `IF_q10_DD`, and `IF_q10_UD`, including mean values of toroidal and poloidal field components. The yellow vertical lines mark the merger time and the black vertical lines mark the time of BH formation.

intervention. The procedure is described in detail in the Appendix. For a quantitative description of the field, we rely instead on histograms of magnetic energy in suitable bins based on spatial position.

An overview of the evolution of the field structure is given in Fig. 7. During early inspiral, the field is given by the initial data prescription, Eq. (1). We recall that the magnetic field strength drops to zero towards the surface
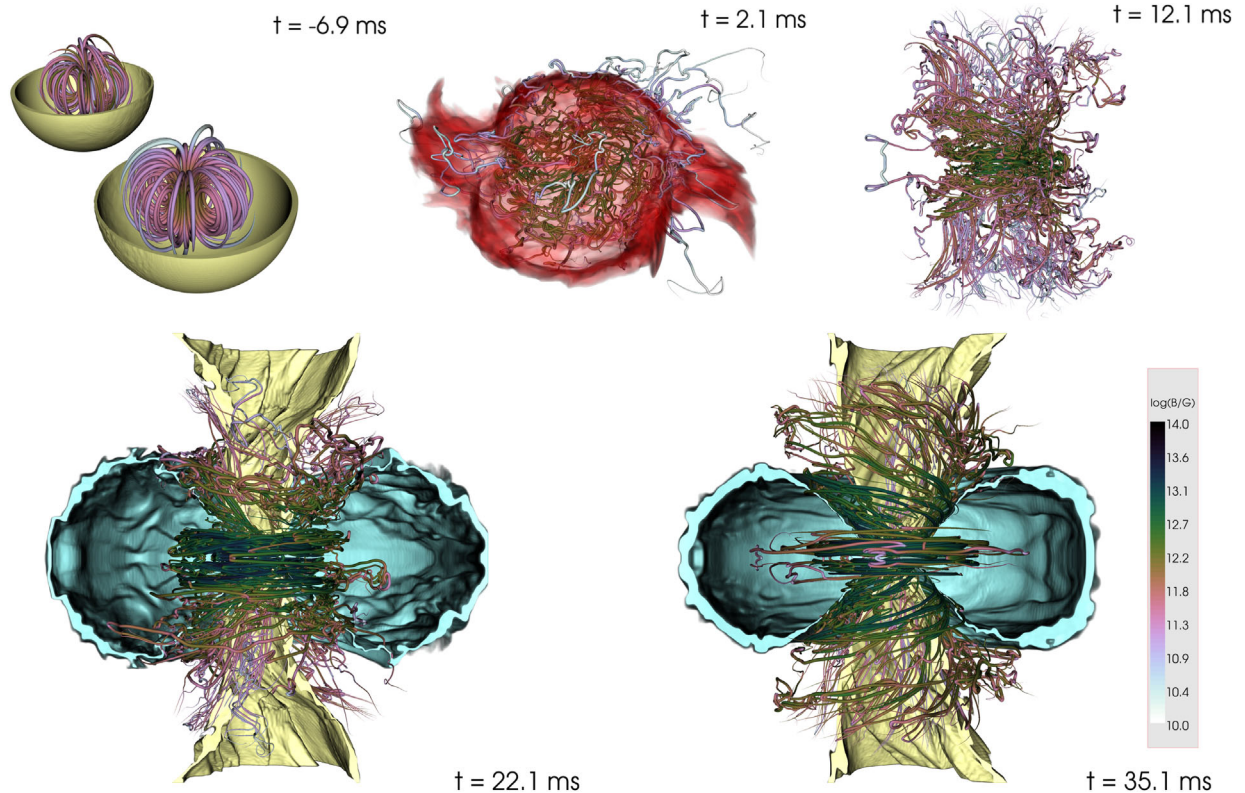

FIG. 7.   Evolution of the magnetic field structure for model `IF_q10_UU`. Top left: Inspiral phase, showing the magnetic field, as well as the lower half of the NS surfaces. Top center: Magnetic field 2 ms after merger together with the isodensity surface for 5×10^{12} g/cm^3, drawn as a semitransparent red surface. Top right: Magnetic field structure 12 ms after merger. Bottom left: Magnetic field 22 ms after merger, together with two isosurfaces of density 10^8 (yellow) and 10^{10} g/cm^3 (cyan), cut off for $y < 0$. Bottom right: The same at 35 ms after merger. The color of the field lines gives a rough indication of the field strength (see color bar), but for quantitative results compare Figs. 8, 10, and 15. The procedure for selecting which field lines to plot is described in the Appendix.

and there is no field outside the stars. During the last orbits of inspiral (not shown in the figure), the field already becomes more irregular. The complex fluid flows during merger finally destroy all regularity, as can be seen in the second snapshot ($\sim$2 ms after merger). In the remaining evolution, the field structure becomes more regular again. As expected, magnetic winding produces a toroidal field of increasing strength near the equatorial plane. More interestingly, we also observe a cone-like region of increasing strength along the edge of the accretion torus. The alignment is highlighted in the figure by displaying two isodensity surfaces in addition to the field. Initially, the field along the cone is more or less tangential, but still relatively irregular. At a later stage, around 30 ms after merger, the lines along the cone acquire a clear "twister" structure. This could be attributed to the stretching of field lines by the fluid flow along the edge of the torus.

By using an interactive version of Fig. 7 to look at magnified parts from different angles, we found that the strong field lines typically turn around sharply at some point and very closely follow their previous path in reverse. This is indeed the expected outcome of stretching an initially irregular field continuously along a quasistationary shearing fluid flow. We stress that Fig. 7 visualizes the orientation of the field, but not the sign, which alternates on small length scales. The cone contains field lines going both upwards and downwards (along the cone), and the toroidal field near the equatorial plane contains field lines wound both clockwise and counterclockwise. The field near the BH axis is only mildly collimated. From animations showing a cut through the meridional plane, we found that it is also strongly fluctuating. This seems to be related to lumps of low-density matter falling towards the BH along the axis.

To quantify the magnitude and topology of the magnetic field, we sum the magnetic field energy contained in bins regularly spaced in $\cos(\theta)$, where θ is the angle to the BH axis. Thus, a homogeneous field would result in a flat distribution. This measure allows us to distinguish the amount of energy in the disk, along the conical structure separating the disk and funnel, and near the axis. As a measure for the strength of the field, we computed for each bin the field strength B_{90}, defined by the requirement that 90% of the magnetic field energy is contributed by regions with field strength below B_{90}. We use this measure because using the maximum field strength is too sensitive to potential outliers, while using the average field strength would depend on the volume under consideration. Using B_{90} is a good compromise.

The energy distribution and the field strength B_{90} for model IF_q10_UU at three different times are shown in Fig. 8. The total magnetic energy near the equatorial plane increases by around an order of magnitude between 12–22 ms after merger, most likely because of magnetic winding in the torus. The energy 35 ms after merger is
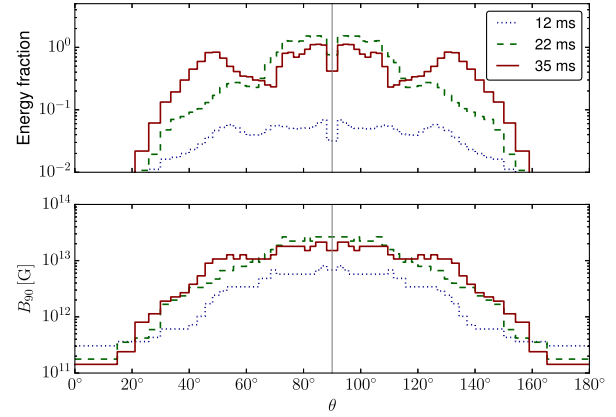

FIG. 8. Distribution of the magnetic field with respect to the θ coordinate, for model IF_q10_UU at various times after merger. Top: Histogram of magnetic energy employing bins regularly spaced in $\cos(\theta)$, where $\theta = 0$ is the z axis and $\theta = 90°$ is the equator. The plot is normalized to the total magnetic energy 35 ms after merger. Bottom: Field strength B_{90} defined as the value for which 90% of the magnetic energy [inside a given $\cos(\theta)$ bin] is contained in regions with field strength below B_{90}.

slightly lower, however. The reason is uncertain, but it might be a change of the torus structure and/or loss by accretion. The energy along the conical structure separating the disk and funnel is steadily growing (side peaks). The final distribution has a pronounced local maximum, corresponding to an opening half-angle around 50°. Notably, the regions near the BH axis ($\theta < 20°$) do not contribute significantly to the total field energy.

The field strength B_{90} near the equator increases from $\approx 6 \times 10^{12}$ G at 12 ms after merger up to $\approx 2 \times 10^{13}$ G at 22 ms after merger, and afterwards it stagnates. B_{90} is of the same order of magnitude at all angles from the equator up to the conical structure, and then it drops rapidly in the funnel. In particular, near the axis the field is very weak (less than 3×10^{11} G at 12 ms after merger), and further drops by a factor of ≈ 2 at the end of the simulation.

B. Comparison with Rezzolla et al. 2011

As mentioned before, the specific choice of EOSs used in this work has been made in order to favor comparisons with previous work. In particular, our equal-mass model employing the simplistic ideal-fluid EOS is the same as the one studied in Ref. [20], the first work to claim the formation of a funnel-like structure in the magnetic field after BH formation, a region of low-density matter where a jet eventually producing a GRB may be launched.

In order to make a meaningful comparison between the present work and Ref. [20], we first describe the differences in the numerical methodology of the simulations. However, we did not investigate the influence of different parameters one by one because it would have been too expensive. Below we report what we believe are the relevant changes.

First of all, in both works the vector potential is the evolved variable for the magnetic field, in order to guarantee the divergence-free character of the magnetic field. However, differently from Ref. [20], we use the modified Lorenz gauge [33,34]. This avoids spurious amplifications of the magnetic field at the boundary between refinement levels, as was observed in the simulations of Ref. [20].

The resolution of the simulation in Ref. [20] is the same as our standard resolution, as is the number of refinement levels. In the current work, we evolved the same model also with higher and lower resolutions, as discussed in Sec. IV H. The location of the outer boundary and the size of the refinement levels are different from Ref. [20]. The finest refinement level after merger in this work only extends to 30 km, compared to 44 km used in Ref. [20]. The outer boundary on the other hand was expanded to 1403 km, almost 4 times the extent used in Ref. [20]. We believe that this was an important improvement on the previous work. The simulation described in Ref. [20] had to be terminated when large spurious waves in the magnetic field coming from the outer boundary had contaminated the solution even near the central object, while we encountered no such problems.

Another difference concerns the symmetries. In both works, a reflection symmetry with respect to the orbital plane was used, but in contrast to Ref. [20], we do not enforce π symmetry around the z axis, thus allowing non-π-symmetric modes to develop. However, in the case of equal-mass binaries the system becomes roughly axisymmetric soon after the merger and therefore we do not think that the different symmetries imposed led to significant differences in the results.

Another improvement is the lower density of the artificial atmosphere in our work, $\sim 6.2 \times 10^4$ g/cm^3, which is 3 orders of magnitude smaller than the one used in Ref. [20]. This could be relevant for the computation of the accretion rate, estimated in Ref. [20] from the time derivative of the total amount of matter outside the apparent horizon, and which might contain a significant error due to the effect of the artificial atmosphere. We measure the accretion rate from the integrated matter flux through the apparent horizon instead.

We now compare the outcome of Ref. [20] to our standard resolution run of the same model. The most important improvement is our detailed analysis of the magnetic field near the BH spin axis. In Ref. [20], a magnetic field of 8×10^{14} G near the axis[1] was reported. In this work, we found a much weaker field near the axis. In fact, we computed the full magnetic field energy spectrum as a function of the angle to the spin axis, and found that 90% of the field energy near the axis (cf. Fig. 8) is contributed by field strengths below 2×10^{11} G, and that the spectrum does not extend beyond 10^{12} G.

Further, we find only a weakly collimated and fluctuating field in this region. We could not reproduce the strong collimation suggested by the field line visualization of Fig. 3 in Ref. [20], which shows field lines originating on the apparent horizon and tracing the shape of the funnel, proceeding outwards nearly as straight lines. One could argue that this is merely a difference in visualization methods, given that the seeds of this plot were selected *ad hoc*, while we adopted a more systematic approach (see the Appendix) for the selection of field lines. However, we do not fully rely on such visualizations and also used two-dimensional (2D) cuts in the meridional plane, both as snapshots and animations, to cross-check our results. What we find instead is a twister-like configuration of the magnetic field, with an opening half-angle around 50° and a field strength around 10^{13} G.

Comparing the evolution of the maximum field strength, i.e., Fig. 4 with the right panel of Fig. 2 in Ref. [20], we find a slightly stronger amplification between merger and collapse. The main difference however is the post-collapse amplification. The maximum field strength in Ref. [20] keeps growing up to 10^{15} G, while for our simulation it settles around 10^{14} G. Also, our simulation is a bit longer and exhibits a decrease of the maximum field strength starting 24 ms after merger. These differences may be due to the different numerical setups of the two simulations, in particular the location of the outer boundary, but we cannot provide certain conclusions.

We stress that the maximum is not a very reliable measure for the growth of the magnetic field, since it is sensitive to outliers, either physical or caused by numerical errors. Inspecting measures not relying on a single point is more meaningful. In particular, the measure B_{90} is a more robust replacement for the maximum. Furthermore, using the density-weighted mean allowed us to quantify the field of the HMNS (see Fig. 5). More specifically, the use of histograms of magnetic energy with respect to the θ coordinate allowed us to quantify the spatial distribution of the post-collapse field in more detail (see Fig. 8). As in Ref. [20], we find a clearly toroidal field structure in the disk, although the maximum strength is more than 1 order of magnitude lower than the value 2×10^{15} G reported in Ref. [20]. Further, the measure B_{90} is around 2 orders of magnitude lower.

Note that a comparison between our Fig. 3 and the left panel of Fig. 2 of Ref. [20] is not possible because they show different quantities: the former shows the total magnetic energy as integrated over the whole domain, while the latter shows the emitted magnetic energy computed by integrating the Poynting vector. We did not compute the latter in our simulation.

---

[1]However, L. B. and B. G. (who are also coauthors of Ref. [20]) found this to be an erroneous statement. The number quoted in Ref. [20] referred to the *global* maximum of the poloidal field component (see also Fig. 2 of Ref. [20]).
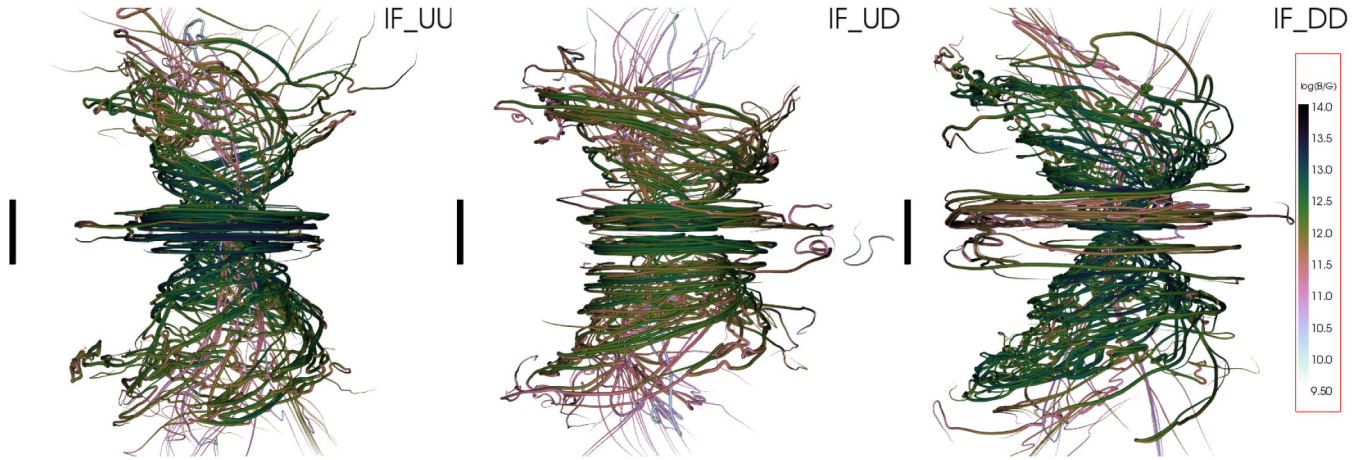
FIG. 9.   Magnetic field structure 35 ms after the merger, comparing models `IF_q10_UU`, `IF_q10_UD`, and `IF_q10_DD`. The black bars provide a length scale of 20 km. The coloring of the field lines indicates the magnetic field strength [$\log_{10}(B[\mathrm{G}])$, with the same color scale for all models] along the lines. However, for quantitative results see Fig. 10.

The mass and spin we found for the BH formed during merger agree better than 1% with Ref. [20]. Also the initial disk mass is comparable. We did however find an accretion rate around 4 times larger than the one reported in Ref. [20]. We believe our result is more robust since we use the flux instead of the total rest mass outside the horizon, which in fact starts *increasing* at some point for the data on which Ref. [20] is based.

Both Ref. [20] and the present work do not find any outflows in the funnel along the rotation axis of the BH. This might be due to missing physical input (neutrino treatment; limits of the MHD approximation) in the simulations and/or too low resolution. We have checked that the matter in the funnel is not magnetically dominated in our simulation, which makes outflows unlikely. We note that the simulations presented in Refs. [19,44] featured mildly relativistic outflows. This is due to the use of stronger initial magnetic fields that allow to better resolve the magnetorotational instability (MRI), and much longer evolutions after BH formation. Finally, Ref. [20] reported some outflows along the edge of the funnel. However, the given limit $\Gamma \lesssim 4$ for the Lorentz factor of the outflows was based on the *global* maximum. Using a movie showing a cut of v^z in the x-z plane ($z > 0$), we find a much lower limit of $v^z < 0.3c$ for any upward movement of matter in the disk or its edge.

C. Effects of the initial magnetic field orientation

When considering a different orientation for the initial magnetic field in the two NSs, we observe almost no differences in the overall dynamics, as well as the final BH mass and spin, the time of BH formation, the mass in the disk, and the accretion rate. Nevertheless, some differences can be observed in the magnetic field evolution. From the magnetic energy and the maximum field strength (Fig. 3 and 4) we see that the totally aligned (with respect to the

orbital axis) or totally misaligned cases—`UU` and `DD`, respectively—reach the same level of magnetic field amplification at the end of the simulation (although with a slightly different path). The case in which magnetic fields are aligned in one NS and antialigned in the other (`UD`) is instead disfavored because of a less efficient amplification in the disk, after BH formation. From the density-weighted average of the magnetic field strength (cf. Fig. 5), we notice a stronger magnetic field amplification in the inner (highest-density) region of the accretion disk for the `UU` case, compared to the `DD` and `UD` cases.

The influence of the initial alignment on the final structure of the field is shown in Fig. 9. All models exhibit the same general features, namely, a toroidal field near the equatorial plane, a twister-shaped field forming a conical structure, and a very weak field near the axis. The relative strength between the cone and equatorial parts seems strongly affected by the initial alignment. This impression is validated by Fig. 10, which shows the distribution of the
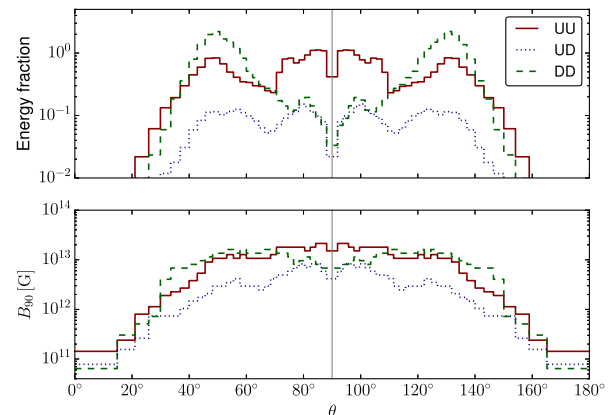

FIG. 10.   Like Fig. 8, but comparing models `IF_q10_UU`, `IF_q10_UD`, and `IF_q10_DD` 35 ms after the merger. The energy distribution (top panel) is normalized to the total energy for model `IF_q10_UU`.

magnetic energy and the field strength B_{90} introduced in Sec. IV A. The UU configuration contains more energy near the equatorial plane than both the UD and DD configurations, which are comparable in that respect. The amount of energy in the cone, on the other hand, is largest for the DD case and smallest for the UD case. The latter also has the weakest field strength B_{90}.

D. Ideal-fluid unequal-mass model

In order to investigate the effect of the mass ratio on the dynamics of matter and magnetic fields, we also evolved a model with a mass ratio of ∼0.8 (model IF_q08).

The bottom rows of Figs. 1 and 2 show the evolution of the rest-mass density on the equatorial and meridional planes, respectively.[2] In this case the evolution is strongly asymmetric with the less compact star being strongly deformed and disrupted during merger. Even if this model has the same total baryonic mass as the equal-mass case, it promptly forms a BH after merger and therefore does not produce a HMNS. It is already evident from Fig. 1 that the disk formed after merger has higher densities and it is more extended. As expected it is indeed more massive than the one formed in the equal-mass case and it has a rest mass of ∼0.21$M_\odot$ at the end of the simulation. The accretion rate is more than 3 times larger than in the equal-mass case, while the BH has a smaller mass and spin (see Table II), due to the larger amount of mass still in the disk by the end of the simulation.

The evolution of the magnetic field strength is shown in Figs. 11–13, and 14. Because of the lack of a HMNS phase, the magnetic field is not amplified to the same maximum strengths as the equal-mass model prior to collapse, but— also because of the fact that more mass is left outside the BH—the density-weighted mean value after BH formation is similar to the equal-mass model (compare the first and second panels of Fig. 14).

The influence of the mass ratio on the structure of the magnetic field is shown in Figs. 15 and 16. For the ideal-fluid models, we find that the magnetic energy near the equatorial plane is reduced by an order of magnitude for the unequal-mass case. The energy and field strength B_{90} in the conical structure are comparable, but the opening half-angle is ≈10° larger for the unequal-mass case. Note that we find much larger differences for the H4 EOS, as will be discussed in Sec. IV G.

E. Equal-mass H4 model

We now investigate the effect of a different EOS using the piecewise approximation of the H4 EOS. We begin by

---

[2]In the central lower panel of both Figs. 1 and 2 one can notice some artificial effects on the boundary between refinement levels, caused by failures in the conservative-to-primitive routine that sets those grid points to atmosphere. These effects, however, are present only in this case and they have a negligible effect on the results discussed in this work.
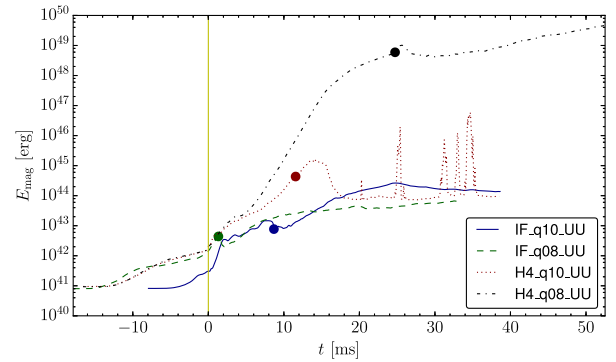

FIG. 11. Comparison of total magnetic energy between models IF_q10_UU, IF_q08_UU, H4_q10_UU, and H4_q08_UU. The yellow vertical line marks the merger time and the circles show the time of BH formation for each model.
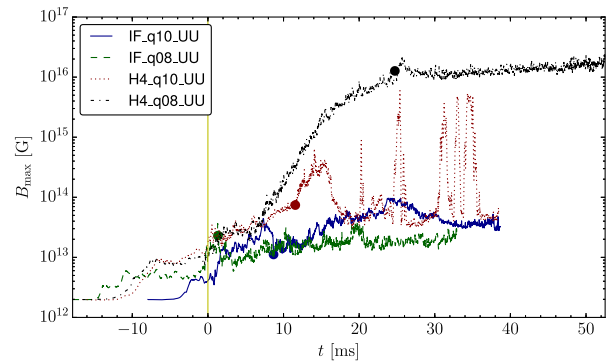

FIG. 12. Comparison of the maximum values of the magnetic field strength between models IF_q10_UU, IF_q08_UU, H4_q10_UU, and H4_q08_UU. The yellow vertical line marks the merger time and the circles show the time of BH formation for each model.

describing our equal-mass model, which we recall is also the same one evolved in Refs. [21,25].

The top panels of Figs. 17 and 18 show the evolution of the rest-mass density on the equatorial and meridional
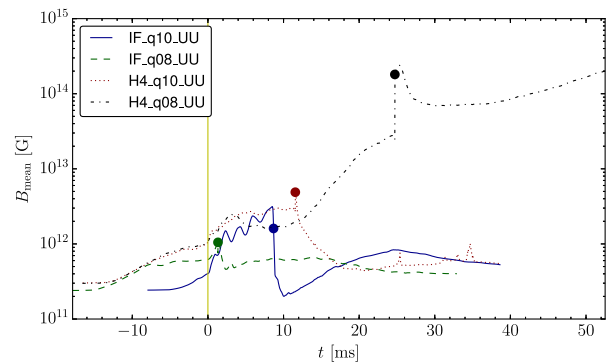

FIG. 13. Comparison of the mean values of the magnetic field strength between models IF_q10_UU, IF_q08_UU, H4_q10_UU, and H4_q08_UU. The yellow vertical line marks the merger time and the circles show the time of BH formation for each model.
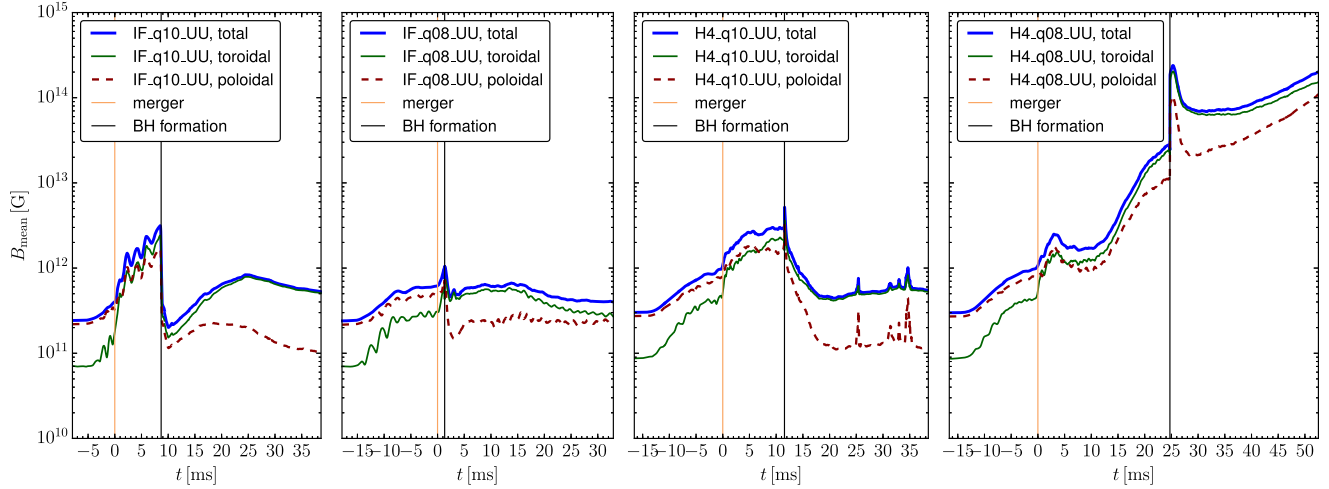
FIG. 14.   Comparison of the mean values of the total, poloidal, and toroidal magnetic field strengths between models `IF_q10_UU`, `IF_q08_UU`, `H4_q10_UU`, and `H4_q08_UU`. The yellow vertical lines mark the merger time and the black vertical lines mark the time of BH formation.
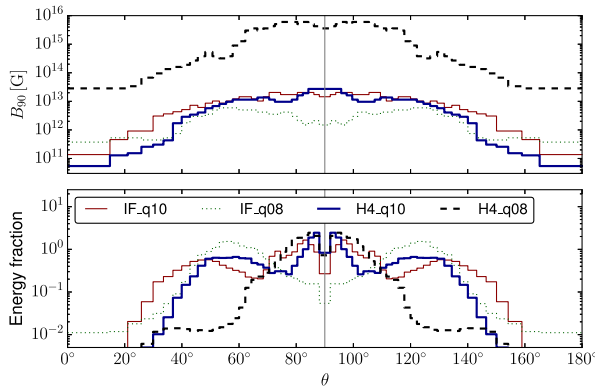

FIG. 15.   Like Fig. 8, but comparing models `IF_q10_UU`, `IF_q08`, `H4_q10`, and `H4_q08` around 32 ms after the merger. Also, each model is normalized separately in the lower panel, and we employ coordinates where the BH is located at the origin to account for the BH drift exhibited by the unequal mass models.

planes, respectively. Like in the case of the ideal-fluid equal-mass model `IF_q10_UU`, the merger remnant goes through a HMNS phase lasting about 12 ms before collapsing to a spinning BH. The disk mass is approximately the same as in model `IF_q10_UU`, but the BH mass is slightly smaller, consistent with the lower initial mass for the H4 models (see Table II).

The comparison of the magnetic field evolution between the H4 and the ideal-fluid equal-mass models is shown in Figs. 11–13, and 14. Since the lifetime of the HMNS is slightly longer than that of the ideal-fluid equal-mass model, the amplification of the magnetic energy and the maximum field strength are larger than in the ideal-fluid equal-mass model during the HMNS phase. After BH formation the magnetic field in the disk has a strength comparable to the one for the ideal-fluid equal-mass model,

even if it exhibits a smaller decrease at BH formation. This may also be correlated with the slightly higher densities in the disk (compare the rightmost top panels of Figs. 17 and 1).

In Fig. 11 one can also notice some spikes in the evolution of the magnetic energy. These are due to very brief amplifications of the magnetic field near the surface of the apparent horizon in matter infalling into the BH and are very rapidly accreted by the BH.

A comparison of the magnetic field structure for models `H4_q10` and `IF_q10` is given in Figs. 15 and 16. Note however that the masses of the stars are also different, not just the EOS. The main difference is the opening half-angle of the conical part of the field, which is $\approx 10°$ larger for the H4 equal-mass case. The magnetic energy and field strength B_{90} are instead very similar (see Fig. 15).

F. Comparison with Kiuchi *et al.* 2014

Our equal-mass H4 EOS model allows for a direct comparison with the results of Refs. [21,25], who studied magnetized binaries with the highest grid resolution to date. For this, they employed a fixed mesh-refinement code described in Refs. [45,46]. The implementation of their fixed mesh refinement (except for the part dealing with the magnetic field) is based on that of the SACRA code [47], which had been quantitatively compared to the WHISKY code [48,49] several years ago in Refs. [50,51]. The main difference between WHISKY and the latest code of Refs. [21,25] is the scheme used to enforce the divergence-free constraint for the magnetic field. Differently from WHISKY, the code of Refs. [21,25] employs a fourth-order-accurate-in-time flux-CT scheme [52], which ensures also the magnetic-flux conservation across refinement boundaries, in addition to the divergence-free condition. Another difference is that the artificial atmosphere density
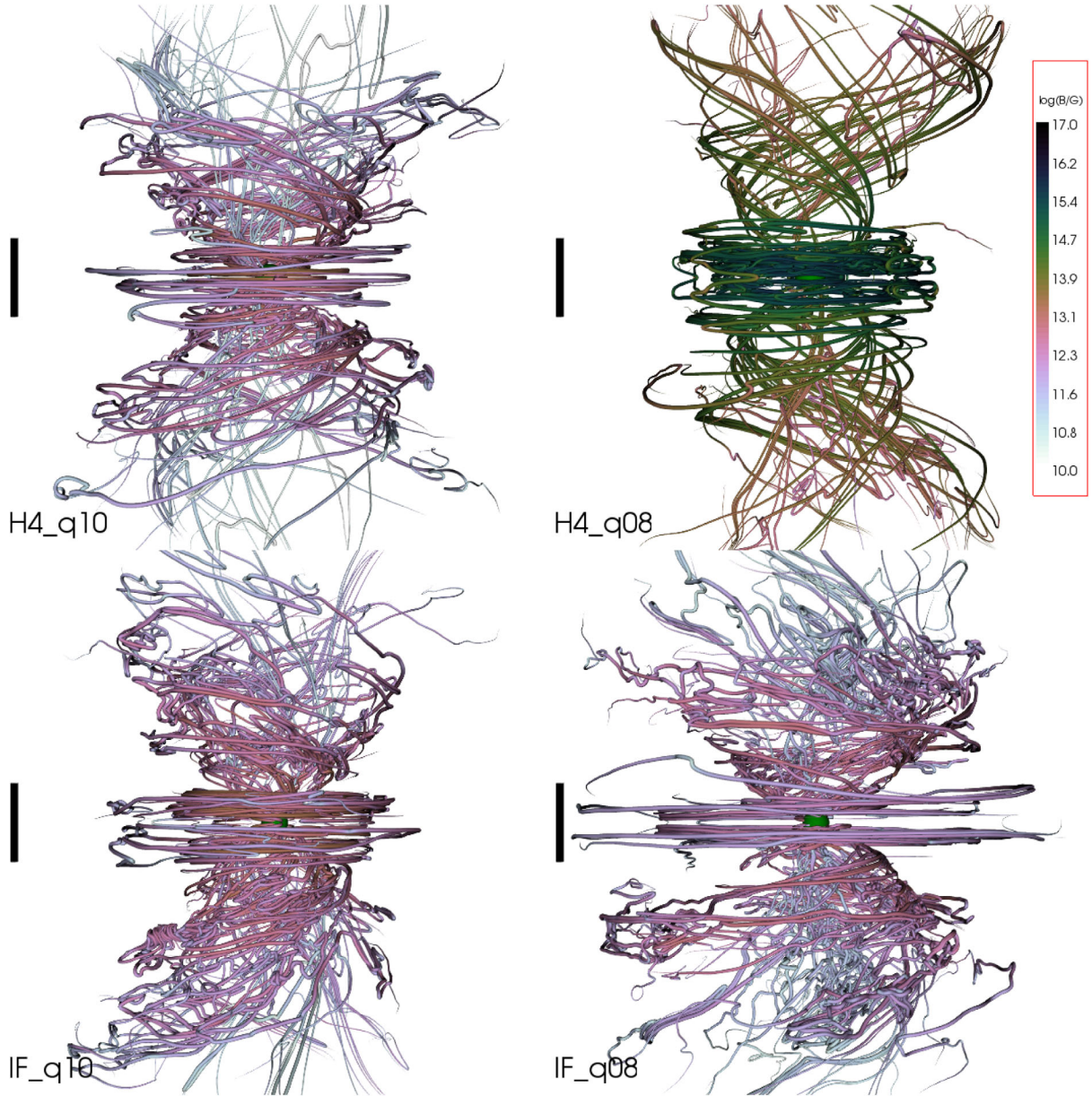
FIG. 16.   Magnetic field structure around 32 ms after the merger, comparing models IF_q10_UU, IF_q08, H4_q10, and H4_q08. The black bars provide a length scale of 20 km. The coloring of the field lines indicates the magnetic field strength [$\overline{\log}_{10}(B[\text{G}])$, with the same color scale for all models] along the lines. However, for quantitative results see Fig. 15.

is only constant up to some fixed radius and then falls of like r^{-2} [46]. This is important for ejected matter and magnetically driven winds, but probably irrelevant for the results discussed here.

The most important difference to the simulations presented in Ref. [21] is the grid resolution. The finest grid spacing used in Ref. [21] is 70 m, which is 2.66 times better than our standard resolution. The extent of the finest level is also larger than ours. The outer boundary in our work is slightly farther out than that in Ref. [21], but this is probably scarcely relevant for the results discussed here. In both cases the computational domain should be large enough to allow the evolution of

the remnant and disk without the influence of boundary effects.

For the equal-mass H4 model, we also performed a simulation with the same grid spacing of 150 m used for the lowest-resolution runs in Ref. [21]. In the following, we compare our main results to the 150 m resolution run in Ref. [21] with the smallest initial magnetic field, 10^{15} G, which is still 500 times stronger than ours. The strong field in Ref. [21] was chosen to facilitate the study of magnetic instabilities, while our aim is to use values more likely to occur in nature.

We find a HMNS lifetime of 10.9 ms, which agrees within 10% with the value shown in Fig. 2 of Ref. [21].
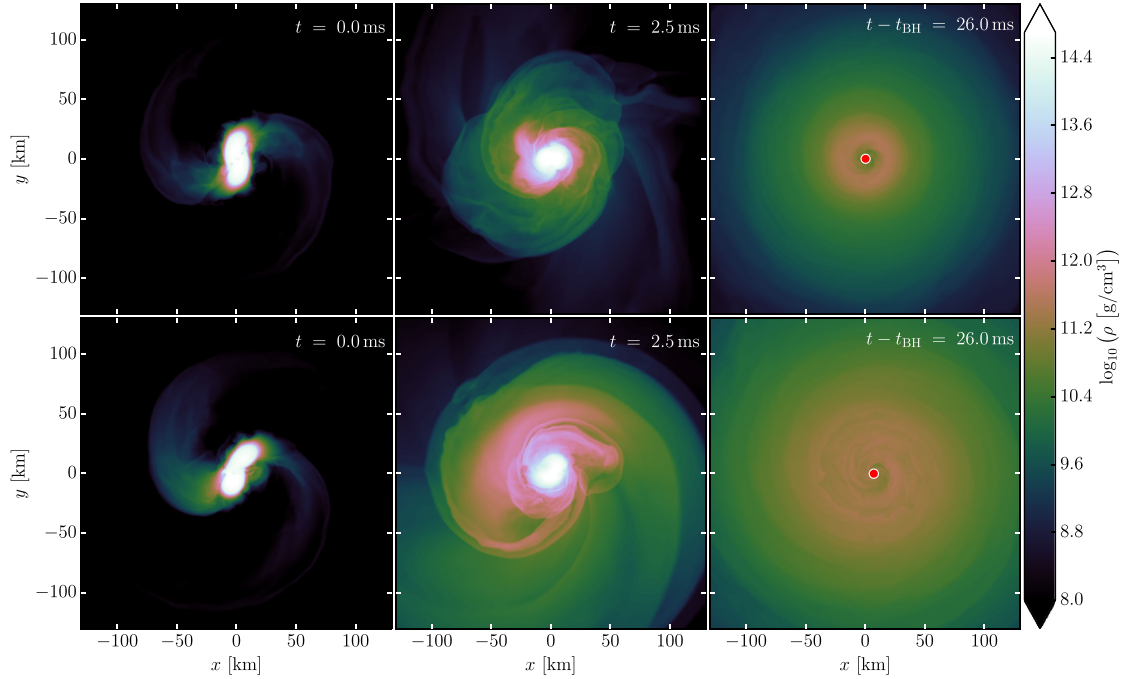
FIG. 17.   Rest-mass density evolution on the equatorial plane for models `H4_q10` (top) and `H4_q08` (bottom).
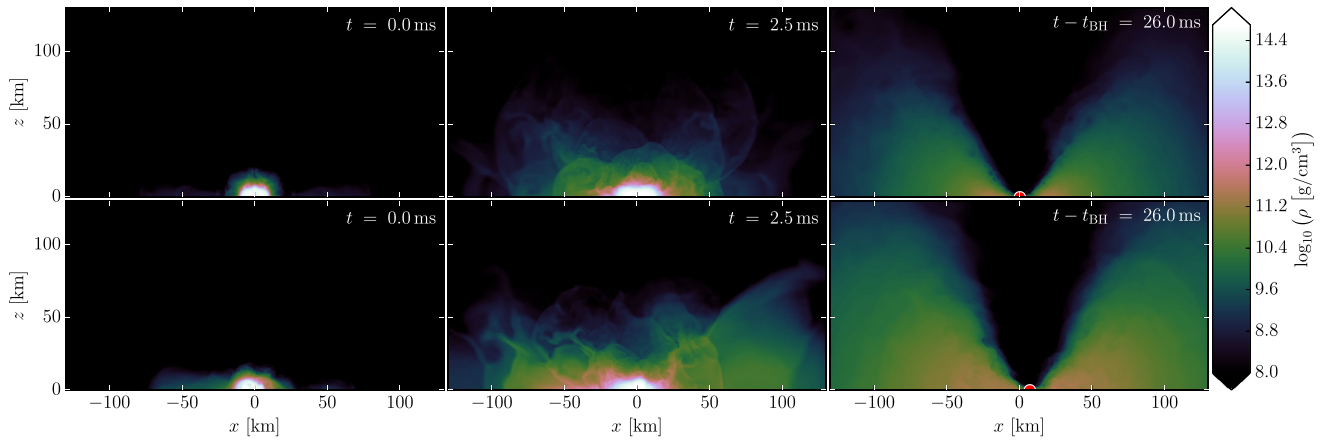

FIG. 18.   Rest-mass density evolution on the meridional plane for models `H4_q10` (top) and `H4_q08` (bottom).

The dimensionless BH spin 10 ms after merger in our simulation is 0.70, which agrees well with the value 0.69 reported in Ref. [21] (albeit for their 70 m resolution run). Also the disk mass of $0.06 M_\odot$ we found (at the same time) is identical to the value given in Ref. [21]. Therefore, the physical conditions for magnetic field amplification are very similar, apart from the different initial field strength.

In our run, the magnetic energy increases from $\approx 10^{43}$ erg at merger time to $\approx 10^{47}$ erg at the time of BH formation. In Ref. [21], the energy is already at this level at merger time and is amplified less than 1 order of magnitude in the 150 m resolution run (in stark contrast to their higher-resolution runs). After collapse, the remaining energy outside the BH

increases from $\approx 10^{47}$ erg up to almost $\approx 10^{49}$ erg, at which point it saturates. In our simulation, the energy first stagnates around 5×10^{46} erg, and then starts growing again around 30 ms after merger, up to a value of 4×10^{49} erg reached 60 ms after merger. We do not observe saturation at this amplitude, but we cannot rule it out at later times. The reasons for the different behavior are unclear. Reference [21] clearly demonstrated that a 150 m resolution is insufficient to resolve the field amplification in the disk, and therefore the differences should not be taken too seriously. That said, we notice that Ref. [21] already reached a slightly higher magnetic energy directly after collapse, which makes it easier to resolve MRI effects in the disk. This might explain the delayed onset of amplification in our case. For more details

about our high-resolution run we refer to Sec. IV H, where the differences with respect to our standard resolution run are discussed.

An important statement in Ref. [21] is that no coherent structure of the poloidal component was found. This contrasts with our results with a lower initial magnetic field. Comparing the field lines shown in Fig. 16 to the ones in Fig. 1 of Ref. [21], we find indeed that the "twister" structure exposed in the former cannot be seen in the latter. On the other hand, the absence of a strongly collimated field along the BH axis reported in Ref. [21] agrees with our findings. The apparent absence of the twister structure might also be an artifact of the different selection of field lines and the larger scale of the plot in Ref. [21], resulting in a lower field line density near the "twister" structure. Furthermore, as described in the Appendix, we made an effort to avoid seeds in the less regular regions between field lines of opposite direction. For those reasons, and also because of the lower resolution of our run, the comparison of the field structure remains rather inconclusive. We note however that our results do not rely solely on the field line plots. Using histograms in Fig. 15, we demonstrate that the dependence of the field energy on the θ coordinate is relatively flat and only falls off strongly between 50–30° around the spin axis.

Finally, we note the study [25], in which additional refinement levels are added, down to a grid spacing of 17.5 m, in order to resolve the Kelvin-Helmholtz (KH) instability during the first few ms after merger. Those results show that a much higher resolution than the one implemented in our simulations is necessary in order to fully resolve the magnetic field amplification due to the KH instability during merger. Therefore, the magnetic field amplification inside the HMNS is most likely underestimated by our runs. The question of how this influences the post-collapse phase is not trivial, since an important fraction of the magnetic energy produced in the shear layer is likely to be swallowed by the BH upon collapse.

G. Unequal-mass H4 model

For the H4 EOS, we found an enormous influence of the mass ratio on the magnetic field amplification (see also Sec. IV H). The total magnetic energy and the maximum of the magnetic field are shown in Figs. 11 and 12 in comparison to the equal-mass H4 model as well as the ideal-fluid models. As one can see, the lifetime of the HMNS (≈ 24 ms) for the H4 unequal-mass case is more than twice as long as that for the H4 equal-mass case. During this phase, the field is growing exponentially, with the exception of the last 5 ms before collapse. The time scale of the exponential growth is also shorter than for the equal-mass case. Shortly before the collapse to a BH, the energy is around 4 orders of magnitude larger than for the equal-mass case, and the maximum field strength is more than 2 orders of magnitude larger. The fact that these

values do not change drastically during collapse implies that most of the energy was contained in regions well outside the HMNS and that the field was also strongest there. As discussed in Sec. IV H, we attribute at least part of this much stronger amplification to the magnetorotational instability.

The amplification after the collapse to a BH is comparable in growth rate to the ideal-fluid unequal-mass case (which showed a prompt collapse after merger). We conclude that the lifetime of the HMNS is a very important factor for the post-collapse field strength in the torus. It is likely that the large differences we see between the ideal-fluid and H4 unequal-mass cases are mostly due to the chosen total mass, i.e., we expect more similar results when comparing H4 and ideal-fluid EOS unequal-mass models with total masses chosen such that the HMNS lifetime is the same. Parameters other than the HMNS lifetime—namely, the disk mass, BH spin, and accretion rate—are comparable to the `IF_q08` case and cannot explain the much larger amplification.

The structure and distribution of the magnetic field 32 ms after merger is shown in Figs. 15 and 16. Apart from the increased amplitude, we find that for the unequal-mass case a larger fraction of the energy is contained in the toroidal field near the equator. The field strength B_{90} reaches $\sim 6 \times 10^{15}$ G near the equator, more than 2 orders of magnitude above the strength for the equal-mass case ($\sim 3 \times 10^{13}$ G). The opening angle of the conical structure is also smaller. As in the equal-mass case, the field near the axis does not contribute significantly to the total magnetic energy, and the field strength B_{90} near the axis is around 2 orders of magnitude below the equatorial value. Due to the overall increase in amplitude, however, this now corresponds to a field strength $B_{90} \approx 3 \times 10^{13}$ G near the axis.

H. Influence of resolution

We performed simulations at different resolutions for the ideal-fluid and H4 equal-mass models (`IF_q10_UU` and `H4_q10`). First we discuss the ideal-fluid case, while the H4 case will be discussed at the end of this section. In the last paragraph, given its particular relevance, we will also discuss the impact of the chosen resolution on the unequal-mass H4 model (`H4_q08`).

Figure 19 shows the evolution of the maximum rest-mass density and magnetic energy at three different resolutions: $dx \approx 177$, 222, and 277 m (where dx is the finest grid spacing). The resolution affects the rest-mass density evolution only in the post-merger phase. The lifetime of the HMNS is extremely sensitive to small numerical errors and numerical convergence is difficult to achieve. In our case, higher resolutions resulted in a longer lifetime, and we see no convergence for the employed resolution range. Note however that in general the lifetime of HMNSs also depends very strongly on their mass.
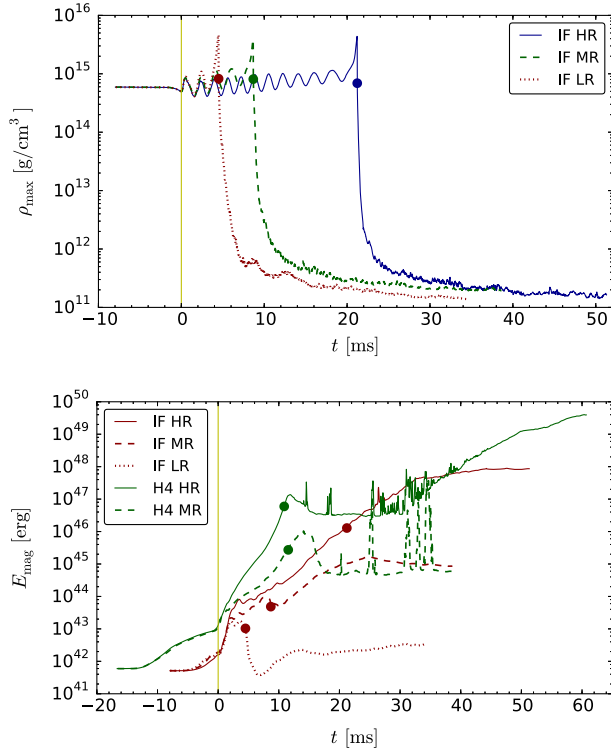
FIG. 19.   Evolution of the maximum rest-mass density (upper panel) and magnetic energy (lower panel) for the equal-mass ideal-fluid model `IF_q10_UU` at different resolutions, with a finest grid spacing of $\overline{dx} \approx 177, 222, 277$ m for the high, medium, and low resolutions, respectively. The evolution of the magnetic energy is also shown for the equal-mass H4 model `H4_q10` with two different resolutions: $dx \approx 150$ m (HR) and 186 m (MR).

The HMNS lifetime directly influences the disk mass, because the strong oscillations of the HMNS in conjunction with the rapid rotation constantly eject matter into the disk. Indeed, the disk mass increases from 0.015 $M_\odot$ for the lowest resolution (and shortest HMNS lifetime) to 0.077 $M_\odot$ at the highest resolution. The mass and spin of the BH on the other hand are only weakly affected by the HMNS lifetime. The differences between high and medium resolution at 30 ms after collapse are both below 1.5%.

During the first ∼2 ms after merger, the magnetic energy shown in the lower panel of Fig. 19 exhibits an exponential increase, with a growth rate that depends only weakly on the resolution. The saturation of this exponential growth on the other hand sets in later (and at higher energies) for higher resolution. This amplification is most likely associated (at least in part) with the KH instability, which can be captured only on scales larger than the grid spacing and therefore is not entirely accounted for in our simulations.

In the subsequent evolution with medium and high resolution, the energy grows exponentially at a comparable rate, but more slowly than directly after merger. We can attribute this to amplification of the field in the disk, since the additional energy is obviously not swallowed into the

BH during the collapse of the HMNS, and because the amplification continues after collapse until it saturates. For the low resolution, the BH forms shortly after merger and the evolution of the field energy is due to the disk afterwards. For all resolutions, the energy increase ceases at some point. With increasing resolution, we observe a longer growth phase and a higher final amplitude. The difference between low and high resolution is more than 5 orders of magnitude. One possible explanation would be that the magnetic field amplification mechanism is acting also on small scales which are better resolved with a finer grid spacing.

One such mechanism that could operate in the disk is the MRI. The wavelength of the fastest growing mode of the MRI is approximately given by $\lambda_{MRI} \approx (2\pi/\Omega) \times B_k/\sqrt{4\pi\rho}$, where Ω is the angular velocity and B_k is the magnetic field strength along the corresponding wave vector. In order to properly resolve this effect the finest grid spacing dx has to cover λ_{MRI} with at least 10 points (see, e.g., Ref. [53]). Figure 20 shows the ratio λ_{MRI}/dx for the highest-resolution run ($dx \approx 177$ m) at the end of the simulation. In this plot, the total magnetic field strength is used instead of B_k, and therefore the given ratio represents an upper limit. The ratio reaches maximum values ≈ 5–10 along the conical structure separating the disk from the funnel, where the magnetic field is the strongest. This indicates that a resolution $dx \lesssim 100$ m would be necessary in order to start resolving the MRI in that region. We note however that our formula for the wavelength does not take into account general-relativistic corrections and uses an idealized disk model.

Saturation of the amplification is not the only possible contribution to the flattening of the magnetic energy growth that happens ∼15–20 ms after collapse. Since the accretion time scale of the disk is ∼50 ms, we can expect that the magnetic energy contained in the accreted matter is relevant. Assuming that the magnetic strength in the inner disk grows as fast as in the remaining disk, the net increase would be zero when the accretion time scale and growth time scale agree. On the other hand, the fact that the maximum field strength and B_{90} saturate as well disfavors
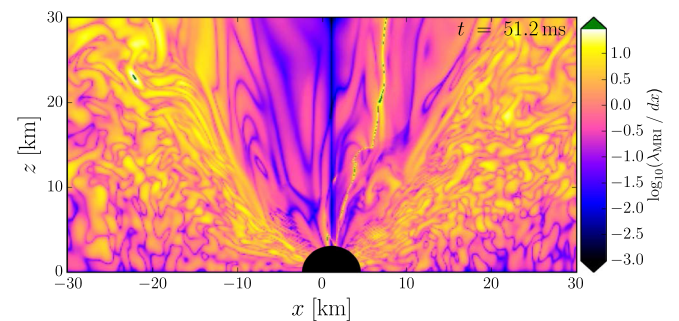

FIG. 20.   Meridional view of λ_{MRI}/dx for the highest-resolution simulation ($dx \approx 177$ m) of model `IF_q10_UU`, towards the end of the simulation ($t = 51.2$ ms).

this scenario. Then again, the change of the disk structure due to accretion could affect the amplification mechanism, which would make the outcome sensitive again to the time of the collapse. The picture is complicated even more by the differences in disk mass due to the different HMNS lifetimes. For those reasons we cannot conclusively associate the flattening of the magnetic energy evolution to an actual saturation of the involved magnetic field amplification mechanisms.

The final magnetic energy between medium and high resolution differs by about 3 orders of magnitude, with the highest-resolution case reaching an increase of more than 6 orders of magnitude in E_{mag} compared to the beginning of the simulation. This amplification factor should be regarded as a lower limit that might be overcome with even higher resolution.

We now turn our attention to the H4 equal-mass model. In this case, we performed simulations at two different resolutions $dx \approx 186$ m (MR) and 150 m (HR). The latter corresponds to the grid spacing employed in the lowest-resolution run of Ref. [21] for a very similar model. A direct comparison has already been presented in Sec. IV F. The lower panel of Fig. 19 shows the evolution of the magnetic energy for the two H4 simulations. In contrast with the ideal-fluid case, there is no significant difference in the time of collapse to a BH (circle markers). Prior to collapse, the magnetic field amplification is stronger in the higher-resolution case, indicating that the dominant amplification mechanisms are not fully resolved. As for the ideal-fluid case, we estimated λ_{MRI}/dx and found that only some isolated lumps inside the "twister" structure are resolved with more than 10 grid points for the high-resolution case. In the highest-resolution run, a further increase in magnetic energy is observed some time after BH formation, corresponding to a strong amplification in the accretion disk. The simulation stops about 50 ms after collapse and we find an overall change in magnetic energy of almost 8 orders of magnitude compared to initial data. This corresponds to an average increase of the magnetic field strength of about 4 orders of magnitude and it could be even larger with higher resolution.

For the unequal-mass H4 model we performed only one simulation with a finest grid spacing of $dx \approx 186$ m. Nevertheless, because the model shows by far the strongest magnetic field amplification (cf. Fig. 11), it is important to assess how well the MRI is resolved in this case. As shown in Fig. 21 and differently from all other models in this study, at the end of the simulation $\lambda_{MRI}/dx > 10$ almost everywhere in the accretion disk. We attribute this to the fact that the magnetic field strength becomes higher because of the much longer lifetime of the HMNS and this makes λ_{MRI} larger. In turn, the MRI is better resolved, leading to a stronger amplification and thus to an even stronger magnetic field. This positive-feedback process provides a likely explanation for the fact that this particular
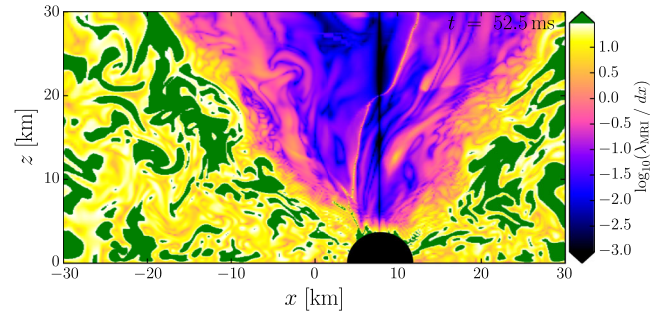

FIG. 21.   Same as Fig. 20 for model `H4_q08` at resolution $dx \approx$ 186 m and at $t = 52.5$ ms.

model ends up with a magnetic energy that is several orders of magnitude higher. However, future simulations at higher resolution will be necessary in order to confirm this picture.

V. SHORT GAMMA-RAY BURSTS AND OTHER ELECTROMAGNETIC SIGNALS

The possibility that the merger of two NSs may be accompanied by an SGRB has been discussed for several decades (see, i.e., Refs. [11,54–56]). The generally invoked scenario is one in which the merger product is a BH surrounded by a massive accreting torus. The rapid accretion of the disk onto the newly formed BH provides the central engine for the burst. Another possibility that has been suggested for powering the engine is the electromagnetic spindown emission from a highly magnetized NS (see, i.e., Refs. [57,58]), which survives for some time before collapsing to a BH or remains as a stable NS (if allowed by its mass [29]). Finally, an alternative "time-reversal" scenario has been proposed [59,60] in which the NS survives for a long time (up to spindown time scales) before eventually collapsing to a BH, and while its rotational energy powers a long-lasting x-ray signal (potentially explaining the x-ray afterglows commonly observed by Swift; see, e.g., Ref. [61]), the SGRB itself is powered by accretion onto the resulting BH, as in the standard scenario. In this work we focus on the first, most studied case in which a BH is formed in less than 100 ms after merger.

The γ-ray emission is believed to be produced within a relativistic outflow (at the distances at which this becomes optically thin), and hence a crucial ingredient of any SGRB model is its ability to drive a jet. Two main mechanisms have been invoked: neutrinos (see, e.g., Ref. [56]) and magnetic fields. At high accretion rates, neutrinos can, in principle, tap the thermal energy of the disk produced by viscous dissipation and liberate large amounts of its binding energy via the $\nu\bar{\nu} \rightarrow e^{+}e^{-}$ process in regions of low baryon density. However, recent simulations of the hyperaccreting disk that include neutrino transfer have shown that, if the remnant torus and environment is that of a BNS merger, then neutrino emission is too short and too weak to yield enough energy for the outflow to break out from the

surrounding ejecta as a highly relativistic jet [62]. Hence, it has been concluded that neutrino annihilation alone cannot power SGRBs from BNS mergers.

On the other hand, a strong poloidal magnetic field around a spinning BH can extract rotational energy and power an outflow [14]. This mechanism is commonly considered the most viable one for producing jets. Therefore, the topology of the post-merger magnetic field in our simulations plays an especially important role. Evidence for a geometrical structure compatible with jet formation in the merger of a BNS was found in Ref. [20], although as already discussed earlier only recently it was possible to show that BNS mergers can actually produce an "incipient jet" along the spin axis of the resulting BH, defined as a collimated and mildly relativistic outflow that is at least partially magnetically dominated [19]. A similar result was obtained earlier for NS-BH binary mergers [44].

Our simulations show the formation of a spinning BH with spin parameter in the range ∼0.6–0.8 (see Table II) and surrounded by a torus of at least a few percent of a solar mass, with the unequal-mass models yielding the larger torus masses. These results are consistent with previous results (e.g., Refs. [15,20]). The average accretion rates are of the order of ∼1 $M_\odot \mathrm{s}^{-1}$. For typical conversion efficiencies of accreted mass to observed radiation, these accretion rates and torus masses satisfy the energy requirements of the observed SGRBs, in particular in the unequal-mass cases [10]. However, the ability to launch a magnetically driven jet requires—in addition to a massive disk—a strong poloidal field along the spin axis of the BH.

As discussed in the previous sections, in our simulations magnetic fields are strongly amplified after merger during the HMNS lifetime (see Figs. 11–12, and 13). Magnetic field amplification continues in the disk after BH formation although in some cases an overall decrease of magnetic energy is observed, possibly due to accretion. As a result of the amplification, and in particular of the winding of the magnetic field lines, the toroidal component becomes dominant over the poloidal one in the disk. Along the edge of the accretion torus we observe the development of a mixed poloidal-toroidal "twister" structure. For the unequal-mass H4 model, we observed a particularly strong amplification of both the poloidal and toroidal components. For this case, the density-weighted mean value grows by over 2 orders of magnitude (see Fig. 14). One important reason for this difference lies in the fact that, for this combination of EOS and NS masses, the HMNS formed upon merger survives for a much longer time scale compared with the other cases that we studied (see Secs. IV G and IV H). The higher torus mass and the stronger magnetic field amplification make the H4 unequal-mass case the most favorable of our models to produce a jet. Also the magnetic field morphology and the half-opening angle of the funnel (smaller than 30°) are compatible with what is needed to drive a SGRB (see Fig. 16 and 18).
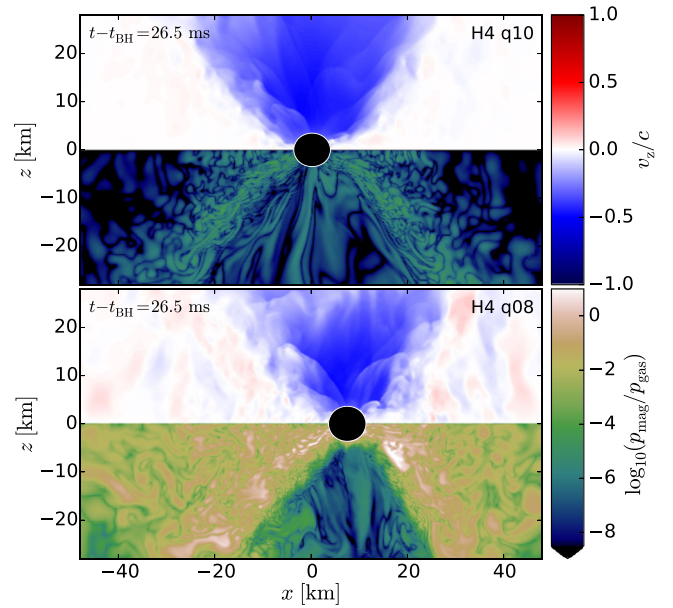

FIG. 22. Meridional view of the BH and accretion torus for the equal- and unequal-mass H4 simulations. The panels refer to 26.5 ms after BH formation and show in the top half ($z > 0$) the fluid velocity along the z axis and in the bottom half ($z < 0$) the magnetic-to-fluid pressure ratio on a log scale.

Figure 22 shows the fluid velocity along the orbital axis and the magnetic-to-fluid pressure ratio[3] for the equal- and unequal-mass H4 simulations, 26.5 ms after BH formation. In both cases matter inside the funnel and along the spin axis of the BH is still infalling and in the unequal-mass case the pressure ratio indicates that the fluid is becoming magnetically dominated at the edges of the disk, but inside the funnel the magnetic field pressure is subdominant. In conclusion, despite the fact that some favorable conditions are met, we do not find evidence of jet formation. Our results confirm the expectation that unequal-mass systems produce more massive disks (for the same total baryonic mass) and we find that longer-lived HMNSs can lead to a much stronger magnetic field amplification, which might also support the formation of a jet.

From our results, we are not in a position to exclude that the systems under investigation can form a jet. Our present simulations are limited to less than 30 ms (in one case 50 ms) after BH formation and an outflow might still emerge on longer time scales. Moreover, magnetic field amplification mechanisms that act on scales that are too small to be properly resolved with our present resolution (such as the Kelvin-Helmholtz instability) would provide much stronger amplification (see, e.g., Refs. [21,25,53]) and thus influence the dynamics.

---

[3]The ratio is defined as $\beta \equiv b^2/(2p)$, where $b^2 \equiv b^\mu b_\mu$ and b^μ is the 4-vector of the magnetic field as measured by the comoving observer [27].

Our simulations lack a neutrino treatment. As such, we cannot compute the contribution of neutrinos to cooling and heating of the remnant disk. Most importantly, our simulations do not allow us to investigate the emergence of a jet driven by neutrino annihilation. However, as discussed above, Ref. [62] concluded that for the BNS merger scenario to yield a SGRB, jets must be magnetically driven. Lacking neutrinos in our treatment should not prevent the simulations from showing the emergence of such a magnetic jet. Nevertheless, neutrinos can still have an impact on the evolution of both the HMNS and the accretion disk.

In addition to the prompt γ-ray emission produced within the relativistic outflow and the associated x-ray and optical afterglows, the merger of two NSs is also expected to create a significant amount of neutron-rich radioactive elements, whose decay should result in a transient signal—the so-called "kilonova" or "macronova"—in the days following the burst (see, e.g., Refs. [63,64]). The emerging radiation is expected to peak in the near IR—due to the large optical opacity of the heavy r-process elements—and to be nearly isotropic. As such, it constitutes an interesting complement to the prompt gamma-ray emission, which is expected to be generally beamed. Kilonova candidates were found to be associated with GRB 130603B [65] (a SGRB at redshift $z = 0.356$), GRB 060614 [66,67], and GRB 050709 [68]. Another promising electromagnetic signal from BNS mergers is the isotropic x-ray emission powered by the spindown of a long-lived NS remnant [69,70], although such a signal is not expected if a BH is formed shortly (<1 s) after merger.

The observation of SGRBs or other electromagnetic counterparts in combination with the BNS merger GW signal will dramatically improve the scientific output of a detection. In the following section we discuss the GW emission from the BNS mergers studied in this work.

VI. GRAVITATIONAL WAVES

For all runs we extract the GW signal at a fixed radius of $\sim$1100 km via the Moncrief formalism (signal is extracted also via the Weyl scalar Ψ_4, but only for cross-checking purposes). Note that extrapolation at infinity is not performed for any of our simulations.

In this section we present the strain of the GW signal as $h_{lm} = h_{lm}^+ + i h_{lm}^\times$, namely, the coefficients of the spin-weighted spherical harmonics expansion. In order to obtain the actual strain that would be measured by a GW detector, one should multiply our value by the spin-weighted spherical harmonics in order to take into account the signal direction. For each simulation we also extracted the instantaneous frequency of the GW from the phase velocity of the complex strain, which is shown in the bottom panels of Figs. 23 and 24.

In Fig. 23 we show the $l = m = 2$ component of the GW strain for models IF_q10, IF_q08, H4_q10, and H4_q08. While in the IF_q08 case (where the system promptly collapses to a BH) the GW includes only inspiral, merger, and ringdown, in all the other cases a HMNS is formed and therefore we also have a longer post-merger GW signal. In the IF_q10 case the GW frequency during the HMNS lifetime varies continuously. This behavior
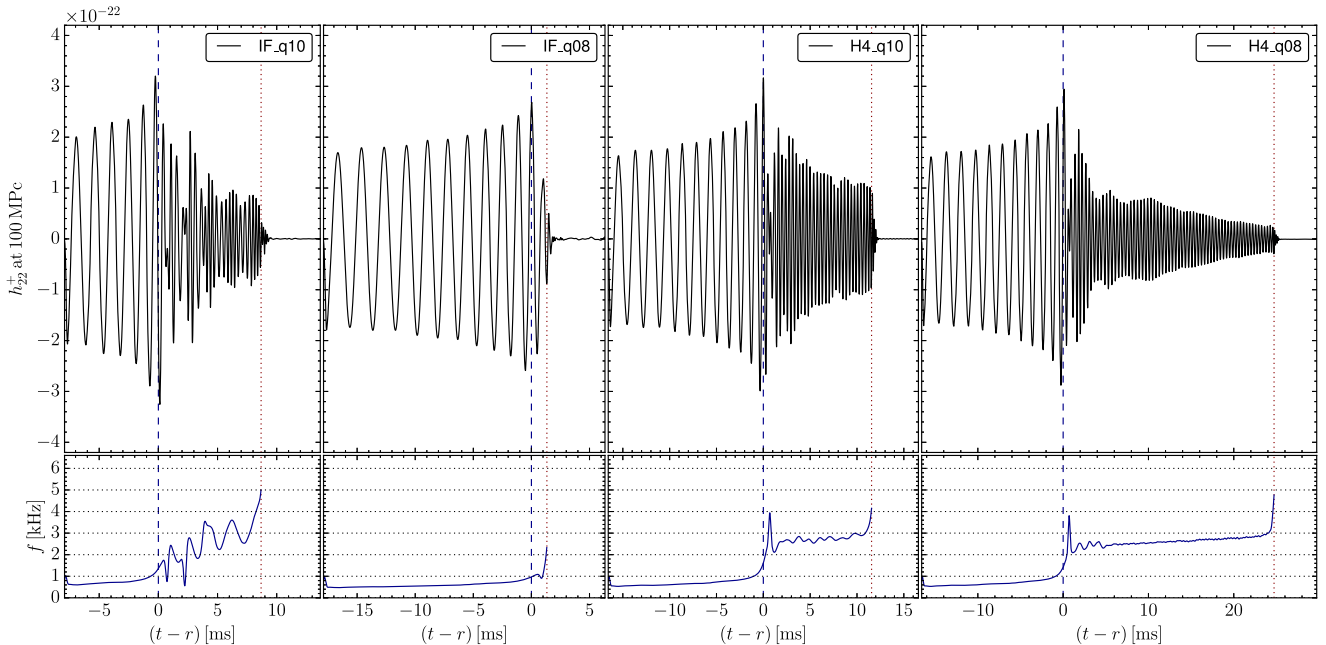

FIG. 23.   GW signal for models (from left to right) IF_q10, IF_q08, H4_q10, and H4_q08. The top panels show the strain at a nominal distance of 100 Mpc. The lower panels show the instantaneous frequency.
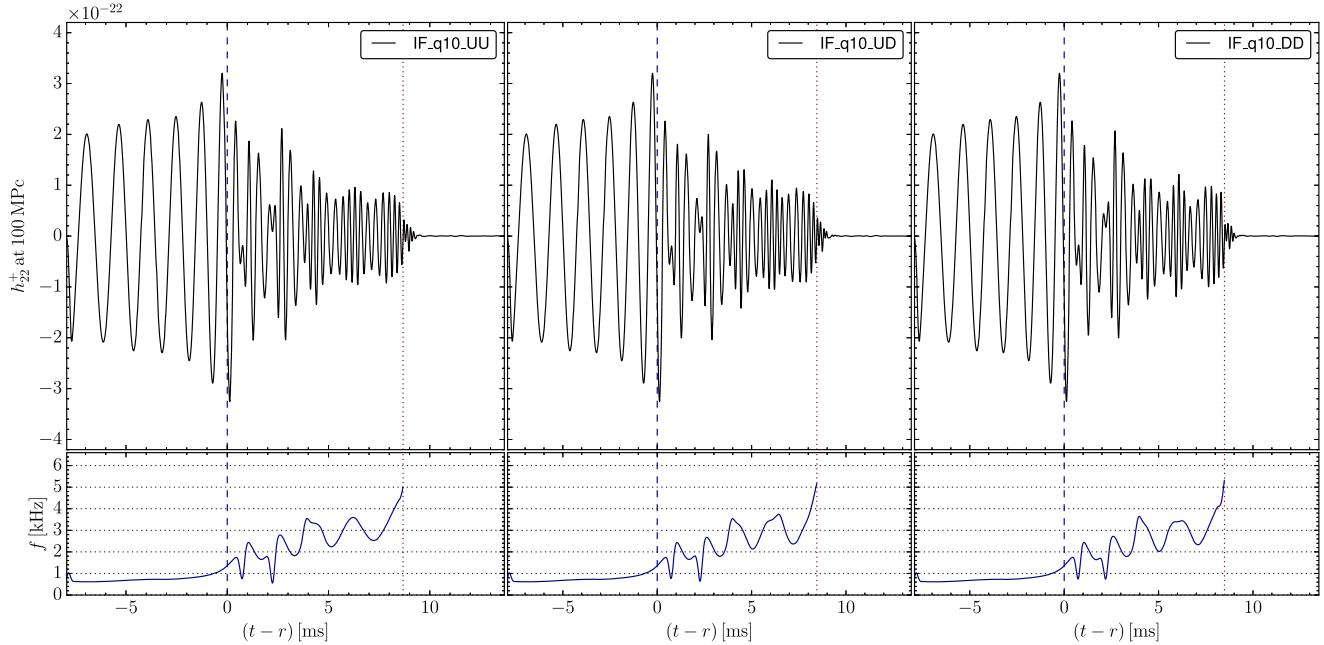
FIG. 24.   GW signal for models (from left to right) `IF_q10_UU`, `IF_q10_UD`, and `IF_q10_DD`. The top panels show the strain at a nominal distance of 100 Mpc. The lower panels show the instantaneous frequency.

differs from the H4 cases, where the HMNS phases show signals with a very strong peak at specific frequencies. Note that in the H4 cases the HMNS has a longer lifetime, and in the H4_q10 case the post-merger GW signal also has a stronger amplitude with respect to the other models. As previously discussed, however, the lifetime of the remnant also depends on the resolution, with the HMNS surviving longer with higher resolution.

In terms of frequency, the H4 models show a drift towards higher frequencies during the post-merger phase, which is more evident in the H4_q08 case, where the remnant lasts longer and the value of the frequency oscillates less. In Table II we report for all models the frequency at merger f_{merger}, and for the H4 cases we report f_{HMNS}, which indicates the frequency corresponding to the most prominent post-merger peak in the GW spectrum (called f_{peak} in Ref. [71] and f_2 in Ref. [72]). We do not

provide f_{HMNS} for the ideal-fluid models since `IF_q08` has no HMNS remnant (it promptly collapses to a BH) and in `IF_q10` the frequency oscillates too much to get an accurate estimate, as it is shown from both the amplitude and spectral behaviors.

We also studied whether the effect of magnetic field orientation had any impact on the GW signal. As shown in Fig. 24, this impact is minimal. This may change if the magnetic field is amplified to much larger values during merger.

Finally, in Figs. 25 and 26 we plot the power spectra of the GW signals for all our simulations against present and future ground-based detector sensitivities (namely, Advanced Virgo, Advanced LIGO, and the Einstein Telescope, all in the standard broadband configuration).

The power spectrum we show in the plots is given by

$$h_{\mathrm{eff}}(f) = \sqrt{\tilde{h}_+^2(f) + \tilde{h}_\times^2(f)}, \text{ where } \tilde{h}_+ \text{ and } \tilde{h}_\times \text{ are the}$$
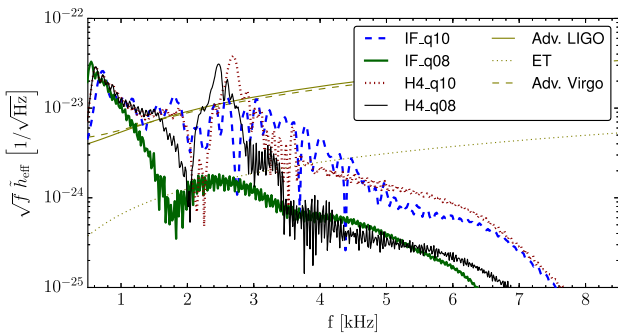

FIG. 25.   GW spectra (solid lines) for the four models of Fig. 23 in comparison to the sensitivity curves of GW detectors (dashed lines). The strain is given at a distance of 100 Mpc.
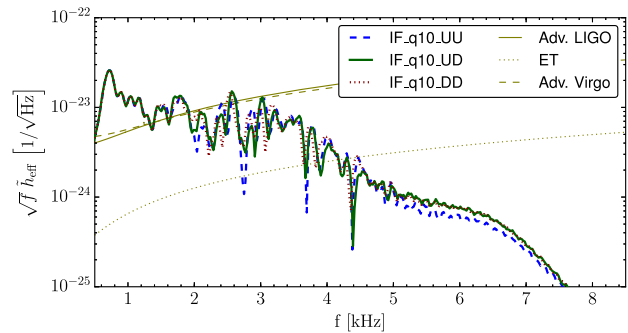

FIG. 26.   GW spectra (solid lines) for the three models of Fig. 24 in comparison to the sensitivity curves of GW detectors (dashed lines). The strain is given at a distance of 100 Mpc.

Fourier transforms of h_{lm}^+ and $h_{lm}^\times$ for $l = m = 2$. From both figures we can see that the inspiral phase would be detected by both Advanced Virgo and Advanced LIGO for all models. Moreover, in Fig. 25 we see that for the H4 models the post-merger peak of the signal due to HMNS oscillations would also be strong enough to be detected by Advanced LIGO and Virgo. If detected, this peak could play a very important role in constraining the NS EOS [71–73].

VII. CONCLUSIONS

In this paper we started our investigation of the magnetic field structure formed in the post-merger of high-mass BNS systems, i.e., of systems that produce a BH on a dynamical time scale after merger. We focused in particular on two different EOSs—ideal fluid and H4—both of which were used recently by other groups to study the merger of equal-mass systems [19–21]. We have extended those previous investigations by including unequal-mass BNSs and by changing (for one configuration) the initial magnetic field orientation.

Compared to previous work, here we have introduced a more systematic way to study the magnetic field structure in order to better understand whether an ordered poloidal field is formed after the merger or not. This has important consequences on the possible formation of relativistic jets and on the central engine of SGRBs.

The main result of this work is that we observe the formation of an organized magnetic field structure after the formation of a BH surrounded by an accretion disk. This happens independently of EOS, mass ratio, and initial magnetic field orientation. The main difference with what was reported by Rezzolla *et al.* [20] is that the field along the BH axis is neither strong nor strongly collimated. We observe a strong field near the edge of the torus, which is not composed of straight magnetic field lines, but instead has a more helical structure, similar to the one observed in Ref. [19]. The initial magnetic field orientation does not produce large differences, but we point out that the UD configuration is the one leading to the smallest amount of magnetic energy and the smallest values for B_{90} along the conical structure separating the low-density funnel and the higher-density disk, where the magnetic field amplification is generically found to be the most efficient. The largest magnetic field is obtained in the unequal-mass model evolved with the H4 EOS (H4_q08). This is due to the much longer HMNS phase in this case which allows for a much larger magnetic field amplification (likely contributed by a better-resolved MRI, cf. Sec. IV H).

We did not observe the formation of a jet in any of the simulations, consistently with what was seen in Refs. [20,21], but this is not unexpected considering the recent results of Ref. [19]. It is indeed known that a magnetically dominated region in the BH ergosphere is a necessary condition for the activation of the BZ mechanism

[14]. On the one hand, our resolution is in general not high enough to be able to fully resolve the KH instability during merger and the MRI after merger (with the possible exception of model H4_q08; see Sec. IV H), and therefore the magnetic field amplification might not be strong enough to activate the BZ mechanism. On the other hand, our simulations are limited to a few tens of ms after BH formation, while it could take longer to realize the conditions to form a jet [19].

A recent study [74] investigated a mechanism where magnetic loops drifting into the BH are inflated and forced to open due to differential rotation between the disk and BH, potentially powering jets. The study assumed the force-free MHD limit as well as axisymmetry, and required a critical size of the initial loops for the case of prograde disks. Therefore it is not clear if this mechanism plays a role in our setup. Future studies can help in assessing the viability of this scenario.

Our next step will be to employ the analysis techniques developed in this paper to study the same (or similar) systems when evolved with our subgrid model [24] or with resolutions that are high enough to better capture KH and MRI. Moreover, we will evolve for a longer time after BH formation. Since in this paper we have shown that the magnetic field structure is qualitatively the same independently of the EOS, mass ratio, and magnetic field orientation, we expect the results of Ref. [19] to be general and we will assess this statement in future simulations.

Another important ingredient will be the use of finite-temperature EOSs and neutrino emission, which were included only recently in GRMHD simulations by another group [30]. These will not produce qualitatively different results, but they will provide a more accurate description of the post-merger phase and GW emission.

Our step-by-step study will help in assessing the individual contributions of the different physical ingredients (high magnetic fields, finite-temperature EOSs, and neutrino emission) to the possible emission of relativistic jets and SGRBs. Initial data used for the simulations described in this paper, as well as gravitational wave signals and movies from our simulations are publicly available online [43].

APPENDIX: VISUALIZING THE FIELD STRUCTURE

Our visualization method for the magnetic field aims at solving the following problems. First, the magnetic field in our simulations is organized in tubes, and the direction of the field between neighboring tubes changes sign. The in-between field is typically weaker and less regular. Using random or regularly spaced seed points for the integration is bound to miss the strong field regions. Second, showing the field lines everywhere leads to visual clutter and obscures the global structure. We therefore have to choose a smaller number of field lines which are representative of the structure. It is important to use a well-defined automated method for the field-line filtering since a biased selection can result in misleading plots. Finding a good selection rule is difficult because the field strength varies strongly between the different parts of the field we are interested in.

To solve the first problem, we divide the volume of interest into a coarse grid (15^3 cells). In each cell, we determine the location of maximum field strength and use it as a seed point. We then integrate the field lines for all seed points. The solution of the second problem is more involved. First, we divide our domain into bins regularly spaced in $\cos(\theta)$, where θ is the angle between the BH axis and the position vector relative to the BH. We then sort the field lines in each bin by their maximum field strength inside the given bin. Next, we assign to each field line the maximum of its rank in all bins it traverses. We then sort the field lines by this "maximum local importance" measure and keep only a given number of them.

This prescription results in a balanced distribution of field lines in the different parts of the field (axis, disk, torus) despite a strongly varying strength on both large and small length scales. One could argue however that the binning in terms of $\cos(\theta)$ might highlight conical structures where there are none in reality. For example, the strong field in the torus casts a "shadow" radially outwards where weaker field lines are not shown. To validate that the visual impression given by the 3D plots shown in this article is correct, we also compared different visualizations, such as volume rendering of the field strength and simple 2D cuts.

[1] B. P. Abbott *et al.* (LIGO Scientific Collaboration and Virgo Collaboration), Phys. Rev. Lett. **116,** 061102 (2016).

[2] B. P. Abbott *et al.* (LIGO Scientific Collaboration and Virgo Collaboration), Phys. Rev. Lett. **116,** 241103 (2016).

[3] R. Perna, D. Lazzati, and B. Giacomazzo, Astrophys. J. **821,** L18 (2016).

[4] A. Janiuk, M. Bejger, S. Charzynski, and P. Sukova, arXiv:1604.07132.

[5] K. Murase, K. Kashiyama, P. Mészáros, I. Shoemaker, and N. Senno, Astrophys. J. **822,** L9 (2016).

[6] L.-X. Li and B. Paczyński, Astrophys. J. **507,** L59 (1998).

[7] S. R. Kulkarni, arXiv:astro-ph/0510256.

[8] B. D. Metzger and E. Berger, Astrophys. J. **746,** 48 (2012).

[9] E. Berger, Annu. Rev. Astron. Astrophys. **52,** 43 (2014).

[10] B. Giacomazzo, R. Perna, L. Rezzolla, E. Troja, and D. Lazzati, Astrophys. J. **762,** L18 (2013).

[11] R. Narayan, B. Paczynski, and T. Piran, Astrophys. J. **395,** L83 (1992).

[12] T. Piran, Rev. Mod. Phys. **76,** 1143 (2005).

[13] E. Nakar, Phys. Rep. **442,** 166 (2007).

[14] R. D. Blandford and R. L. Znajek, Mon. Not. R. Astron. Soc. **179,** 433 (1977).

[15] L. Rezzolla, L. Baiotti, B. Giacomazzo, D. Link, and J. A. Font, Classical Quantum Gravity **27,** 114105 (2010).

[16] M. Anderson, E. W. Hirschmann, L. Lehner, S. L. Liebling, P. M. Motl, D. Neilsen, C. Palenzuela, and J. E. Tohline, Phys. Rev. Lett. **100,** 191101 (2008).

[17] Y. T. Liu, S. L. Shapiro, Z. B. Etienne, and K. Taniguchi, Phys. Rev. D **78,** 024012 (2008).

[18] B. Giacomazzo, L. Rezzolla, and L. Baiotti, Mon. Not. R. Astron. Soc. **399,** L164 (2009).

[19] M. Ruiz, R. N. Lang, V. Paschalidis, and S. L. Shapiro, Astrophys. J. **824,** L6 (2016).

[20] L. Rezzolla, B. Giacomazzo, L. Baiotti, J. Granot, C. Kouveliotou, and M. A. Aloy, Astrophys. J. **732,** L6 (2011).

[21] K. Kiuchi, K. Kyutoku, Y. Sekiguchi, M. Shibata, and T. Wada, Phys. Rev. D **90,** 041502 (2014).

[22] K. Dionysopoulou, D. Alic, and L. Rezzolla, Phys. Rev. D **92,** 084064 (2015).

[23] J. Zrake and A. I. MacFadyen, Astrophys. J. **769,** L29 (2013).

[24] B. Giacomazzo, J. Zrake, P. Duffell, A. I. MacFadyen, and R. Perna, Astrophys. J. **809,** 39 (2015).

[25] K. Kiuchi, P. Cerdá-Durán, K. Kyutoku, Y. Sekiguchi, and M. Shibata, Phys. Rev. D **92,** 124034 (2015).

[26] S. S. Komissarov and M. V. Barkov, Mon. Not. R. Astron. Soc. **397,** 1153 (2009).

[27] B. Giacomazzo and L. Rezzolla, Classical Quantum Gravity **24,** S235 (2007).

[28] B. Giacomazzo, L. Rezzolla, and L. Baiotti, Phys. Rev. D **83,** 044014 (2011).

[29] B. Giacomazzo and R. Perna, Astrophys. J. **771,** L26 (2013).

[30] C. Palenzuela, S. L. Liebling, D. Neilsen, L. Lehner, O. L. Caballero, E. O'Connor, and M. Anderson, Phys. Rev. D **92,** 044045 (2015).

[31] F. Löffler, J. Faber, E. Bentivegna, T. Bode, P. Diener, R. Haas, I. Hinder, B. C. Mundim, C. D. Ott, E. Schnetter,

G. Allen, M. Campanelli, and P. Laguna, Classical Quantum Gravity **29**, 115001 (2012).

[32] L. Anton, O. Zanotti, J. A. Miralles, J. M. Marti, J. M. Ibanez, J. A. Font, and J. A. Pons, Astrophys. J. **637**, 296 (2006).

[33] Z. B. Etienne, V. Paschalidis, Y. T. Liu, and S. L. Shapiro, Phys. Rev. D **85**, 024013 (2012).

[34] B. D. Farris, R. Gold, V. Paschalidis, Z. B. Etienne, and S. L. Shapiro, Phys. Rev. Lett. **109**, 221102 (2012).

[35] A. Harten, P. D. Lax, and B. van Leer, SIAM Rev. **25**, 35 (1983).

[36] P. Colella and P. R. Woodward, J. Comput. Phys. **54**, 174 (1984).

[37] A. Endrizzi, R. Ciolfi, B. Giacomazzo, W. Kastaun, and T. Kawamura, Classical Quantum Gravity **33**, 164001 (2016).

[38] T. W. Baumgarte and S. L. Shapiro, Phys. Rev. D **59**, 024007 (1998).

[39] M. Shibata and T. Nakamura, Phys. Rev. D **52**, 5428 (1995).

[40] T. Nakamura, K. Oohara, and Y. Kojima, Prog. Theor. Phys. Suppl. **90**, 1 (1987).

[41] N. K. Glendenning and S. A. Moszkowski, Phys. Rev. Lett. **67**, 2414 (1991).

[42] J. S. Read, B. D. Lackey, B. J. Owen, and J. L. Friedman, Phys. Rev. D **79**, 124032 (2009).

[43] See Supplemental Material at http://link.aps.org/supplemental/10.1103/PhysRevD.94.064012 for initial data, gravitational wave signals, and movies from our simulations.

[44] V. Paschalidis, M. Ruiz, and S. L. Shapiro, Astrophys. J. **806**, L14 (2015).

[45] K. Kiuchi, S. Yoshida, and M. Shibata, Astron. Astrophys. **532**, A30 (2011).

[46] K. Kiuchi, K. Kyutoku, and M. Shibata, Phys. Rev. D **86**, 064008 (2012).

[47] T. Yamamoto, M. Shibata, and K. Taniguchi, Phys. Rev. D **78**, 064054 (2008).

[48] L. Baiotti, I. Hawke, P. Montero, and L. Rezzolla, in *Computational Astrophysics in Italy: Methods and Tools*, Vol. 1, edited by R. Capuzzo-Dolcetta (MSAIt, Trieste, 2003), p. 210.

[49] L. Baiotti, I. Hawke, P. J. Montero, F. Löffler, L. Rezzolla, N. Stergioulas, J. A. Font, and E. Seidel, Phys. Rev. D **71**, 024035 (2005).

[50] L. Baiotti, M. Shibata, and T. Yamamoto, Phys. Rev. D **82**, 064015 (2010).

[51] J. S. Read, L. Baiotti, J. D. E. Creighton, J. L. Friedman, B. Giacomazzo, K. Kyutoku, C. Markakis, L. Rezzolla, M. Shibata, and K. Taniguchi, Phys. Rev. D **88**, 044042 (2013).

[52] D. S. Balsara and D. S. Spicer, J. Comput. Phys. **149**, 270 (1999).

[53] D. M. Siegel, R. Ciolfi, A. I. Harte, and L. Rezzolla, Phys. Rev. D **87**, 121302 (2013).

[54] B. Paczynski, Astrophys. J. Lett. **308**, L43 (1986).

[55] D. Eichler, M. Livio, T. Piran, and D. N. Schramm, Nature (London) **340**, 126 (1989).

[56] M. Ruffert and H.-T. Janka, Astron. Astrophys. **344**, 573 (1999).

[57] Z. G. Dai, X. Y. Wang, X. F. Wu, and B. Zhang, Science **311**, 1127 (2006).

[58] B. D. Metzger, E. Quataert, and T. A. Thompson, Mon. Not. R. Astron. Soc. **385**, 1455 (2008).

[59] R. Ciolfi and D. M. Siegel, Astrophys. J. **798**, L36 (2015).

[60] R. Ciolfi and D. M. Siegel, *Proc. Sci.*, SWIFT10 (2015) 108, arXiv:1505.01420.

[61] A. Rowlinson, P. T. O'Brien, B. D. Metzger, N. R. Tanvir, and A. J. Levan, Mon. Not. R. Astron. Soc. **430**, 1061 (2013).

[62] O. Just, M. Obergaulinger, H.-T. Janka, A. Bauswein, and N. Schwarz, Astrophys. J. **816**, L30 (2016).

[63] S. Rosswog, Astrophys. J. **634**, 1202 (2005).

[64] B. D. Metzger, G. Martínez-Pinedo, S. Darbha, E. Quataert, A. Arcones, D. Kasen, R. Thomas, P. Nugent, I. V. Panov, and N. T. Zinner, Mon. Not. R. Astron. Soc. **406**, 2650 (2010).

[65] N. R. Tanvir, A. J. Levan, A. S. Fruchter, J. Hjorth, R. A. Hounsell, K. Wiersema, and R. L. Tunnicliffe, Nature (London) **500**, 547 (2013).

[66] B. Yang, Z.-P. Jin, X. Li, S. Covino, X.-Z. Zheng, K. Hotokezaka, Y.-Z. Fan, T. Piran, and D.-M. Wei, Nat. Commun. **6**, 7323 (2015).

[67] Z.-P. Jin, X. Li, Z. Cano, S. Covino, Y.-Z. Fan, and D.-M. Wei, Astrophys. J. **811**, L22 (2015).

[68] Z.-P. Jin, K. Hotokezaka, X. Li, M. Tanaka, P. D'Avanzo, Y.-Z. Fan, S. Covino, D.-M. Wei, and T. Piran, arXiv:1603.07869.

[69] D. M. Siegel and R. Ciolfi, Astrophys. J. **819**, 14 (2016).

[70] D. M. Siegel and R. Ciolfi, Astrophys. J. **819**, 15 (2016).

[71] A. Bauswein and H.-T. Janka, Phys. Rev. Lett. **108**, 011101 (2012).

[72] K. Takami, L. Rezzolla, and L. Baiotti, Phys. Rev. Lett. **113**, 091104 (2014).

[73] K. Takami, L. Rezzolla, and L. Baiotti, Phys. Rev. D **91**, 064001 (2015).

[74] K. Parfrey, D. Giannios, and A. M. Beloborodov, Mon. Not. R. Astron. Soc. **446**, L61 (2015).